



Utrecht University

VAN 'T HOFF LABORATORY FOR PHYSICAL & COLLOID
CHEMISTRY

SOFT CONDENSED MATTER & BIOPHYSICS

An experimental study of the versatile motility of autophoretic droplets

Master's thesis by:

BERTJAN J.M. VAN DIJK BSC

Supervisors:

PEPIJN G. MOERMAN MSC

PROF. DR. WILLEM K. KEGEL

PROF. DR. ALFONS VAN BLAADEREN

Saturday 22nd December, 2018

Abstract

Where equilibrium systems can be almost completely described by classical thermodynamics, out-of-equilibrium processes are not fully grasped. Active materials function as model systems to study those out-of-equilibrium phenomena. Self-propulsion is an example of a non-equilibrium process in biological systems that cannot in full detail be comprehended using state-of-the-art thermodynamics. But some synthetically built particles can self-propel as a result of their surface properties and reactivities. Janus colloids, of which one side is coated with a catalyst, tend to swim due to the catalytic reaction on their surface. Other particles, so called isotropic droplets that are not asymmetrically coated, can (above a critical Péclet number) propel themselves as a result of a spontaneous symmetry-breaking in their solute gradient. The excretion leads to an inhomogeneity in the surface-tension at the surfactant stabilised droplet surface, resulting in Marangoni flow. Here we show our findings concerning the type of motion performed by these autophoretic droplets. Their solute gradients influence the neighbouring fluid flow and are capable of enhancing and propelling these droplets, producing flow patterns that are abundantly studied throughout the literature.

List of Abbreviations

CHT	Circle Hough transform
CMC	Critical micelle concentration
CsMC	Critical swollen micelle concentration
DEP	Diethyl phthalate
ID	Inner diameter
MSD	Mean square displacement
OD	Outer diameter
PIV	Particle image velocimetry
PS	Polystyrene
SDS	Sodium dodecyl sulfate
VCF	Velocity correlation function
WLF	Williams-Landel-Ferry

Nomenclature

α	Rotation angle with respect to horizontal x-axis (perpendicular to gravity)
a	Particle radius, also horizontal axis variable in parameter space
A	Activity or expulsion rate
A_c	Cross-sectional area
b	Slip-velocity coefficient, also vertical axis variable in parameter space
c	Concentration
c_s	Concentration of surface molecules
c_∞	Concentration of bulk molecules
C_d	Drag coefficient
d	Dimensionality
D	Stokes-Einstein (translational) diffusion coefficient
D_H	Hydraulic diameter
D_r	Rotational diffusion coefficient
\hat{e}	Unit vector along the intrinsic direction
φ	Rotation angle with respect to initial swimming direction
f_D	Darcy friction factor
F_d	Drag force
F_g	Gravitational force
F_N	Normal force
g	Acceleration due to gravity
h	Height
η	Viscosity
η_d	Viscosity of the droplet
η_f	Viscosity of the fluid
θ	Inclination angle
k	Geometric factor
k_B	Boltzmann constant ($= 1.38 \cdot 10^{-23} \text{ J} \cdot \text{K}^{-1}$)
K	Adsorption length
λ	Characteristic potential range
L	Characteristic length (typically the particle radius) and capillary length
L^*	First moment of solute distribution
M	Particle mobility
M_o	Molecular mass of the oil
M_w	Molecular weight
N	Number of time steps
N_o	Number of oil molecules
N_s	Number of surfactant molecules
p	Pressure
P	Perimeter
Pe	Péclet number
Pe_{cr}	Critical Péclet number
ρ	Density
r	Radial distance or particle radius

R	Capillary radius
σ_S	Symmetry number
τ_r	Orientational correlation or persistence time
t	Time
t_B	Ballistic time
t_D	Diffusion time
t_{ref}	Reference time characteristic for a specific problem
T	Temperature (in case of WLF equation in degrees centigrade)
u	Particle or flow velocity, also flow velocity in horizontal x-direction
U	Characteristic velocity
v	Flow velocity in the vertical y-direction (perpendicular to gravity)
v_B	Average ballistic velocity
v^s	Slip-velocity
w	Flow velocity in the z-direction (parallel to gravity)
Y^s	Potential (slip-velocity) function

Preface

At the start of this master's research, I hardly knew anything about fluid dynamics and the closest thing I experienced related to it was the water flowing out of the tap in the laboratory. Therefore, even the possibility of visualising the flow at the micro-level seemed very distant but at the same time very intriguing to me.

Towards the end of the bachelor's my field of focus gradually switched from organic to physical chemistry. For this reason I decided to broaden my knowledge of physics by having a closer look inside the Van 't Hoff Laboratory, specifically by applying some of the computational skills acquired during the undergraduate part of my studies.

This plan was made possible by a research proposal set up by Pepijn Moerman, who had the idea of investigating the type of motion of self-propelling droplets and their influence by the surrounding fluid flow profile. In this thesis several experimental disciplines in physics (microfluidics, fluid dynamics) are combined with computational analysis and a little chemistry in an attempt to relate the quantified motion to the flow in close proximity to the droplet.

A challenging topic that would not have been possible without the help of a fair few talented scientists. First of all my daily supervisor Pepijn, thank you very much for your constructive help, experience and your great deal of patience, even when I was at the worst position (I literally lost all my data), you helped me to regain my data, provide me with new insights and motivated me to attempt new procedures.

Willem Kegel, the king without a crown, absolutely easy going, funny (I've heard, but never experienced ☺, grapje!), and doing his very best to welcome everyone in his group. I'm very thankful for accepting me in your research group, for your help and insights in mine and other's topics during the brainstorm sessions. Your jovial approach and good mood always resulted in an open and cheerful environment.

Alfons van Blaaderen, we came across a little less, but the moments I had questions you were there to give a detailed explanation. I would like to thank you for giving me the opportunity to do research in your group and letting me use some of most advanced materials your lab has to offer. Then Jan Groenewold, the theoretician from prof. Kegel his group, who continuously kept on bringing new ideas, approaches and insights in a didactic supportive manner, thank you for your contribution.

Furthermore from the brainstorm session, I would like to thank Jasper Landman for helpful theoretical discussions, and Ivan Rehor and Michele Zanini for their help with experimental approaches. Bonny Kuipers and Peter Helfferich are acknowledged for technical assistance as well as both the Physical & Colloid Chemistry and the Soft Condensed Matter & Biophysics groupmembers for the nice time in either of these groups.

Also my gratitude towards Laís Soares Lavra for ongoing emotional and theoretical support, as well as to my friends and family, more specifically my parents Klaas and Rita who both have done everything within their capabilities to support all of their children on the intellectual, emotional and financial level. Sometimes you have been receiving nothing but complains and frustration, but all of us are extremely grateful for your unconditional love and support, thank you!

Contents

Contents	vi
1 Introduction	1
2 Hydrodynamic enhancement below the swimming threshold	4
2.1 Introduction	4
2.2 Theoretical background	7
2.2.1 Stokes flow	7
2.2.2 Marangoni flow	7
2.2.3 Sedimentation	8
2.2.4 Microfluidics	10
2.2.5 Particle tracking	11
2.3 Materials and methods	13
2.3.1 Surfactant (stock) solution preparation	13
2.3.2 Microfluidics	13
2.3.3 Sedimentation experiments	13
2.3.4 Characterisation	14
2.4 Results and discussion	14
2.4.1 Passive and enhanced sedimentation	14
2.4.2 Droplet shrinking	14
2.4.3 Experiments compared to predictions	16
2.4.4 Sedimentation results	18
2.5 Conclusions	19
3 Self-propulsion above the critical Péclet number	20
3.1 Introduction	20
3.2 Theoretical background	21
3.2.1 Mean square displacement	21
3.2.2 Velocity autocorrelation function	21
3.2.3 Rotation angles	22
3.2.4 Particle image velocimetry	23
3.2.5 Types of fluid flow fields	24
3.2.6 Velocity decays	25
3.2.7 Symmetry number	25
3.3 Materials and methods	26
3.3.1 Surfactant solution preparation	26
3.3.2 Microfluidics	27
3.3.3 Experiments	27
3.3.4 Characterisation	27
3.4 Results and discussion	29
3.4.1 Microfluidic size control	29
3.4.2 Swimming dynamics of various sized droplets	29

3.4.3	Quantifying the motion of various sized droplets	30
3.4.4	Visualised flow around various sized droplets	33
3.4.5	Average flow profiles of various sized droplets	35
3.4.6	Radial decay of the (tangential) velocity	36
3.4.7	Relating the droplet motion to the fluid flow	38
3.5	Conclusions	41
4	Conclusions	42
	Bibliography	43
	Appendix	47
A	Fabrication of microfluidic devices	47
B	Particle tracking algorithm	49
C	Fabrication of the sedimentation sample well	53
D	The relation between Navier-Stokes and Reynolds	54
E	Flow velocities in microfluidic devices	56

Chapter 1

Introduction

Complex systems typically are built up by distinct members, of which the individual behavior is understood, but the *collective behavior* of the system is much more complicated to fully grasp. This phenomenon is known as emergence and is studied thoroughly throughout a wide range of disciplines. [1, 30]

An example system for studying collective behavior is self-assembly, where individual particles find each other without interference by an external guiding source and form patterns. Self-assembly can be distinguished in two variations: static and dynamic self-assembly. In static self-assembly particles gather due to Brownian encounters and stick as the systems tends to attain its lowest possible energy state, realising thermodynamic equilibrium. In dynamic self-assembly particles are studied that act out-of-equilibrium and therefore fall beyond our descriptions of the equation of state.

Multiple non-equilibrium systems exist. Nowadays popular systems studied by biologists, chemists and physicists are active matter. That are systems that take up energy from their environment and turn it into mechanical motion. Numerous biological systems are capable of self-propelling themselves, which according to Edward Purcell demand a non-reciprocal movement [10, 31], defined as a symmetrical movement.

Generally speaking, we take autonomously behaving matter (so without any interference from an external force) to be active. In nature active matter can range from full-grown mammals to insects, but also organs and bacteria are among them. The state-of-the-art knowledge of these complex systems is lacking to suffice in a full-covering mathematical description, meaning that we have to start at the basics and consider a simplistic system.

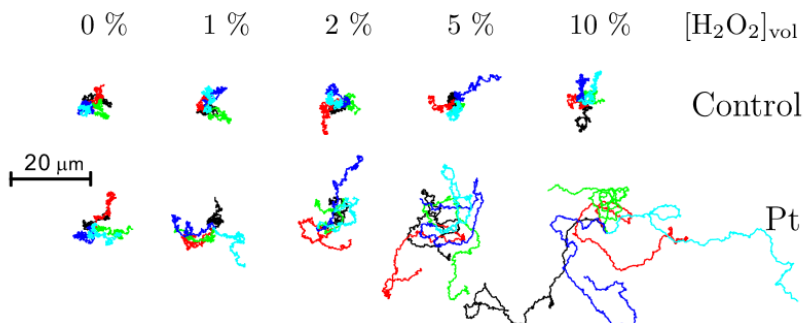


Figure 1.1: Coated and uncoated particle trajectories at multiple reactant concentrations, a figure taken from the paper of Howse et al. [13].

An active process from biology is the autonomous movement of cells. The cell responds to

a chemical gradient (e.g. food/fuel) and moves by means of flagella or cilia. This response-driven propulsion of biological cells is called chemotaxis, and has similarities to the self-propulsion studied in this thesis. In chemistry and physics less complicated systems are studied as chemists and physicists possess the knowledge to (theoretically) create such simple model systems and study their behaviour [13, 16, 36].

Chemists are able to provide us with a synthetic version of actively behaving matter (here called active particles) and gain insight about their non-ideal behaviour by visually investigating their actions. Active particles exist in various shapes and sizes: like spheres [13, 26], disks [15] and rods [27]. They are studied in bulk [39], at interfaces [40] or in confinement [19] and can for example be triggered by: magnetic attraction or repulsion [26], by light [26] or electrical charges [38].

Whereas motion caused by thermal gradients are studied [32] in for instance Leidenfrost droplets. The focus of this study will merely lie on solute gradients caused by differences in surface tension, i.e. the Marangoni effect. But first a quite well-understood active particle has to be discussed, namely the Janus colloid [11, 13, 26, 40]. This colloid owes its name to the bifacial Roman god of duality: Janus, as it is partly coated with a catalyst.

When reactants react faster on the catalytic surface of a Janus particle than reaction products diffuse away, product will locally build up. Diffusion will tend to homogeneously spread the reaction products whereas the catalytic surface will create new product. If there locally lacks a fresh supply of reactant, the colloid will move to new places where reactants are abundant. The interplay between hydrodynamics and gradient formation leads to self-propulsion of the Janus particle.

Janus particles can be produced using a wide variety of catalysts which drive different reactions, so various combinations between catalysts and support materials can be thought of. However the platinum catalysed decomposition of H_2O_2 is among the most frequently mentioned in literature. Typical particle trajectories for different hydrogen peroxide concentrations are shown in figure 1.1 [13]. Besides asymmetrically coated Janus spheres there also exist isotropic spheres capable of self-propulsion.

Thutupalli et al. [36] are among the first to publish about these autophoretic droplets, that move as a result of the solute gradient formed by the bromination of a nonionic surfactant at the droplet surface. Where Thutupalli showed reaction-based propulsion of an aqueous droplet in oil, Izri et al. [16] shared the observed trajectories of pure water droplets in oil (figure 1.2a). All that is necessary for the system of Izri et al. is oil, water and detergent to stabilise the mixture. The driving force is also a solute (swollen micelles) gradient.

Janus particles have a predetermined side at which the reactant gradient forms, whereas in the

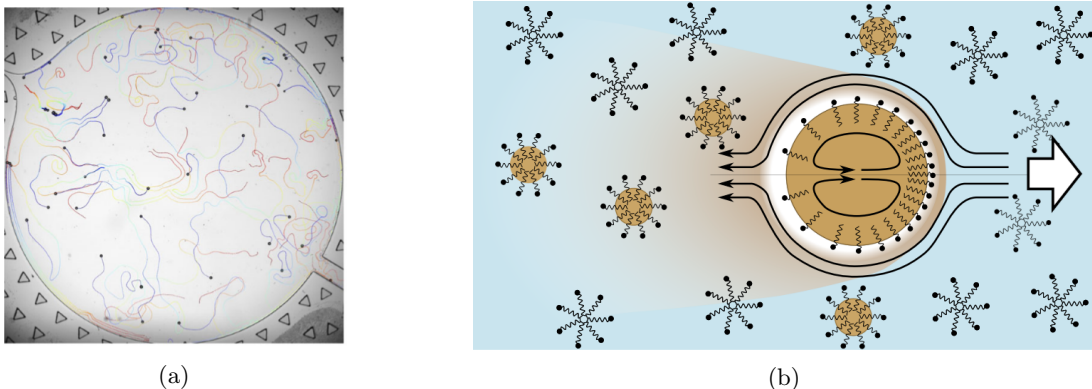


Figure 1.2: In 1.2a Izri et al. show trajectories (recorded for 500 seconds) of centimeter sized water droplets in oil that are driven by the formation of reverse micelles. In 1.2b we schematically see how such (reverse) micelles are formed as a result of Marangoni flow at the droplet surface. Figure 1.2b is a typical illustration above the CMC from the paper by Jin et al. [17].

case of isotropic droplets swollen micelle formation (shown in figure 1.2b) happens isotropically. As generally the droplet (or particle) is pushed away by its solute gradient, Janus particles have a predetermined swimming direction (which can change direction in high salt concentrations [5]), whereas isotropic droplets do not have a "fixed" direction.

In Chapter 2 the focus will lie on slow droplet dissolution, and the effect the formed gradient has on the sedimentation velocity. In Chapter 3 the focus lies on fast dissolution and the resulting self-propulsion. The general conclusions are drawn in Chapter 4 and some side information that was not immediately necessary for the understanding of this thesis is given in the appendices.

Chapter 2

Hydrodynamic enhancement below the swimming threshold

2.1 Introduction

The swimming direction of self-propelling droplets is not predetermined by their surface properties. The solute gradient formation on isotropic droplets will occur isotropically, and therefore does not have an intrinsic direction. If enough surfactant is solubilised in a fluid, the molecules will tend to agglomerate and form micelles, which will happen above of a certain critical micelle concentration (CMC). If micelle formation happens in the presence of a lyophobic¹ substance, the micelles will tend to shield this substance. It is thermodynamically favourable for the micelles to take up some of the substance, resulting in swollen micelles.

The formation of swollen micelles occurs even under the CMC. In a situation where lyophobic solutes are present in solution, it is thermodynamically favourable to screen the lyophobic solutes from the surrounding solution even though the CMC is not reached. This phenomenon is well-known when two or more immiscible fluids are brought together in the presence of surfactant molecules. Swollen micelle formation is encountered in our system of interest, consisting of an oil called diethyl phthalate (DEP) dispersed in water containing a surfactant named sodium dodecyl sulfate (SDS), of which the CMC ≈ 8.2 mM at 25 °C [24].

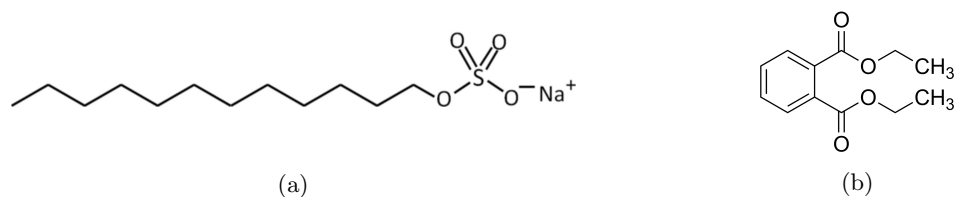


Figure 2.1: In 2.1a we see the molecular structure of sodium dodecyl sulfate and in 2.1b the structure formula of diethyl phthalate is shown.

An oil droplet in an aqueous environment is shielded from the surrounding hydrophilic nature by SDS surfactant molecules. The twelve-carbon long tail sticks into the oil whereas the polar sulfate group remains in the water resulting in an interface between oil and water. Above the critical swollen micelle concentration (CsMC) it is more favourable to form swollen micelles instead of having dissolved surfactant monomers and a stabilised oil "reservoir". Even though several solutes are present, our system behaves and therefore will be described as an incompressible Newtonian fluid.

¹Lyophobic means "solvent hating" and is applicable for any type of solvent.

In an aqueous surfactant solution in which oil droplets are dispersed (above the CsMC), the tendency to take up tiny amounts of oil from the large "reservoir" droplet and form swollen micelles is most favourable [37]. Upon formation of these swollen micelles, a gradient is formed. Similar to what is observed around the Janus colloids, the gradient is built up locally and has to diffuse away in order to obtain homogeneity. Here we come across two competing time scales, namely the time it takes for advection to transport swollen micelles versus the time it takes the swollen micelles to diffuse away.

Here we express the ballistic time scale $t_B \propto \frac{a}{v_B}$ as the time it takes for advection to transport fluid in a straight line over a length given by the droplet radius. The diffusive time scale is expressed as the time it takes for the swollen micelle to diffuse away the droplet's radius $t_D \propto \frac{a^2}{D}$. In these equations a is the droplet radius, v_B the average ballistic velocity and D the Stokes-Einstein translational diffusion coefficient. The Péclet number is a dimensionless ratio between these two time scales and is described as the ratio between the diffusive transport rate versus the advective transport rate.

$$\text{Pe} = \frac{t_D}{t_B} = \frac{UL}{D} = \frac{AaM}{D^2} \quad (2.1)$$

At time scales $t_D \gg t_B$, advection is much faster than diffusion and this corresponds to a $\text{Pe} \gg 1$, which results in self-propulsion. For consistency with later descriptions we take v_B to be a characteristic velocity U and take the droplet radius a to be a characteristic length L and obtain the well-known form for mass transfer. The $\text{Pe} = \frac{UL}{D}$ form is also given by the product of the Reynolds number ($\text{Re} = \frac{\rho UL}{\eta}$), that tells something about the ratio between inertial and viscous forces, and the Schmidt number ($\text{Sc} = \frac{\eta}{\rho D}$), that relates the viscous diffusion to the mass diffusion.

The expression on the right-hand side of equation 2.1 is introduced by Michelin [21] as a specific definition for isotropic droplets. Here A is the surface activity, a the droplet radius and M the mobility of the droplet as a result of the gradient. Since the mobility and the diffusion coefficient are constants [16] in the Péclet number, the left-over variables are the droplet radius and the activity. According to the supplementary information of the paper by Moerman et al. [22, 23] the activity or expulsion rate is given by $A = \frac{N_s}{N_o} \frac{\rho}{M_o} \frac{\partial a}{\partial t}$, meaning that the activity is proportional to the rate of droplet shrinking $A \propto \frac{da}{dt}$.

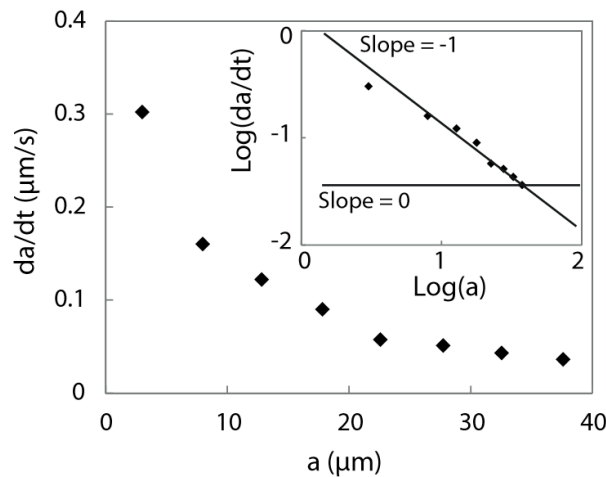


Figure 2.2: Rate of shrinking of a DEP droplet in a 5 mM SDS solution plotted against the particle size, note that in this image a is not the particle radius. The inset shows a slope of -1 in the log-log representation which implies a diffusion-limited dissolution [22].

In figure 2.2, which is a courtesy of Pepijn Moerman, the expulsion rate is plotted against the droplet size. From this figure we see that the decrease goes with $\frac{1}{a}$, meaning that the droplet shrinking depends on the curvature and thus is diffusion-limited. Considering that the Péclet number is related to a constant $c = \frac{M}{D^2}$ multiplied by the droplet radius and its activity $Pe = caA$. Since the activity scales with the curvature, we can effectively say that the Péclet number is independent of the droplet size.

Knowing the droplet size and the rate of shrinking, a Péclet number can be calculated by which the droplet shrinking can be related to the diffusion of swollen micelle. Now as the Péclet number is proportional to the rate of shrinking, and the rate of shrinking depends on the surfactant concentration (more surfactant means more fuel and therefore faster dissolution and thus faster shrinkage), we can relate the Péclet number to the surfactant concentration. Moerman et al. found that the Péclet number scales linear with the SDS concentration, therefore $Pe \propto [SDS]$.

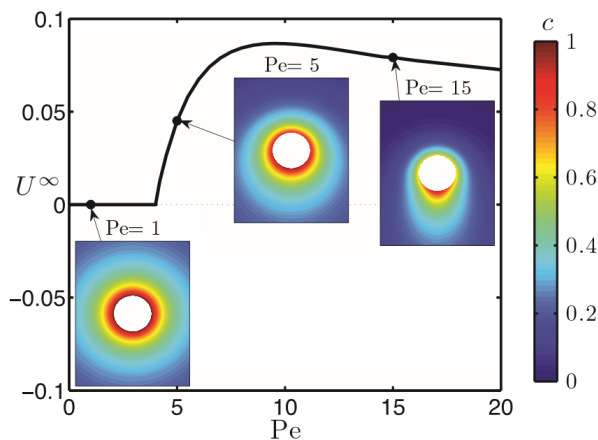


Figure 2.3: Modified figure originating from Michelin’s paper [21] stating that above a critical Péclet number ($Pe_{cr} = 4$) a spontaneous symmetry breaking in the solute concentration occurs that will result in self-propulsion.

For small values of the Péclet number (say $Pe \approx 1$) advection and diffusion occurs according to similar time scales and therefore no propulsion is expected whilst there clearly is dissolution of the isotropic droplet. Michelin et al. predicted a threshold value for the Péclet number, what we will call the critical Péclet number, above which self-propulsion is expected and calculated this value to be $Pe_{cr} = 4$ (figure 2.3). When the Péclet number exceeds this threshold value a spontaneous symmetry breaking in the accumulating solute concentration is expected, resulting in directional motion.

In this chapter we will break the symmetry of the surfactant gradient surrounding the droplet by means of gravity and investigate the influence to droplet propulsion. Theoretical predictions for the sedimentation velocities of passive and active droplets were done [22], and will be verified by sedimentation experiments at different surfactant concentrations below the critical Péclet number. The main question we attempt to answer here, is whether gradient formation below the critical Péclet number can cause enhancement of the sedimentation velocity?

To collect reliable data the idea is to use relatively small ($< 35 \mu\text{m}$) monodisperse droplets in order to measure considerably long trajectories (> 5 seconds) for determining the average sedimentation velocity, as well as to provide us with enough information to obtain a shrinking rate. Microfluidics will be introduced to produce monodisperse droplets, whereas it will be shown that particle tracking is an appropriate tool for the determination of both the sedimentation velocities and the rates of shrinking.

2.2 Theoretical background

2.2.1 Stokes flow

Michelin et al. predicted that isotropic droplets are capable of swimming above a critical value of the Péclet number. We will look at sedimentation velocities below this critical value, in order to see if gradient formation leads to enhancement. Sedimentation velocities of our isotropic droplets depend on the Reynolds number, and this number results from the Navier-Stokes equation. In Appendix D is shown how the Reynolds number depends on the Navier-Stokes equation.

The description for the sedimentation velocity used in this thesis is only valid in the low Reynolds regime. In the low Reynolds limit viscous forces dominate over inertial forces and the Navier-Stokes equation is reduced to the Stokes equation. The fluid flow around our (sedimenting) droplets is described by the Stokes equation, that is written as:

$$\vec{\nabla} p = \eta \nabla^2 \vec{u}. \quad (2.2)$$

This is the equation solved by Michelin et al. [21] for the two cases that required solutions, namely the flow inside and the flow outside the droplet. In order to be able to determine the droplet motion relative to the flow, and perturbations involving this flow field, a series of steps have to be considered and solved. Solving the Stokes equation for both cases goes beyond the framework of the research, but can be briefly commented.

Starting with the expulsion rate at the droplet interface, it is assumed that the surfactant that flows at this interface equilibrates fast [3] and that material exchange between the fluid and the interface is negligible [18]. This problem of surface dissipation, when solved, can then serve as an appropriate boundary condition at the surface of the droplet, giving the opportunity to solve the hydrodynamic Stokes equation of both sides of the interface.

Michelin solved the autophoretic framework and found that above a critical value of the Péclet number a spontaneous symmetry-breaking occurs. Above this value he observed droplet velocities relative to the surrounding flow field, and therefore predicted that self-propulsion of isotropic particles is possible above a critical Péclet number.

2.2.2 Marangoni flow

We now have seen that the Reynolds number can tell us something about the type of forces that play a role concerning a moving particle. We can all understand that Janus particles propel as a result of an asymmetrical gradient formation, but propulsion of isotropic droplets is much trickier. "Isotropic particles cannot swim unless they are large enough for a symmetry-breaking instability involving advection of the surrounding chemical field, [...]" according to Sébastien Michelin and Eric Lauga [20].

Theoretically some assumptions need to be made in order to be able to compile a framework. Chemical self-diffusiophoresis of isotropic swimmers is induced by the chemical tendency to stabilise hydrophobic oil by shielding it with a thin layer of surfactant. In the autophoretic framework this layer is infinitely thin, and oil molecules pass through it. Above a certain critical concentration it is favourable to subduct small amounts of oil from the initial droplet and shield their hydrophobicity in a micellar environment. This critical concentration is denoted as the CsMC which lies around 4 mM SDS.

At sufficiently high surfactant concentrations, droplet dissolution results in the formation of a swollen micelle gradient. Rapid dissolution above the critical Péclet number leads to a spontaneous symmetry-breaking in the swollen micelle (or surfactant) gradient, which results in self-propulsion. Provided that a symmetry-breaking occurs, micelle formation is now more abundant on one side of the droplet. Simultaneously it means that when more swollen micelles are extracted on one side compared to the other, a smaller amount of surfactant molecules are covering that part of the surface.

Upon swollen micelle formation surfactant molecules are taken away from the droplet surface. Since there appear empty sites on the droplet surface there is a gradient in surfactant molecules,

and therefore in surface tension. In order for the SDS molecules on the surface to homogenise, a surfactant flow on the droplet surface is induced. This flow at the fluid-fluid interface is called Marangoni flow and is caused by a gradient in surface tension. As this Marangoni flow slips the advection stream at the interface, we can express Marangoni flow as a slip-velocity, which according to John Anderson [3] can be equated as

$$v^s = -b\vec{\nabla}Y^s. \quad (2.3)$$

Here ∇Y^s stands for the gradient of a potential function like in this case the solute concentration. The slip-velocity coefficient b that represents the material properties of the surface is in the case of diffusiophoresis of nonionic chemical species given by $b = \frac{k_B T}{\eta} KL^*$, in which K represents the adsorption length and L^* the first moment of solute distribution. If we assume this distribution to be an Boltzmann distribution that is dependent on some potential energy, the combination of these variables results in a variable best described as a characteristic potential range λ .

Michelin defined the droplet mobility $M = \frac{k_B T}{\eta} \lambda^2$ in a solute gradient as a material property of isotropic droplets [21]. Here λ relates to K and L^* , which for the y-variation can be taken as $\lambda^2 = KL^* = \int_{-\infty}^{\infty} y (c - c_{\pm}^s) dy$. A small remark needs to be made, since the interface between the droplet and the solvent is defined at $y = 0$, $1/\eta$ needs to be taken into the integral as for the the positive values we look into the solution with the viscosity of water, and for the negative values we look into the droplet so there the viscosity of oil is considered.

$$v^s = -M\vec{\nabla}c = -\frac{k_B T \lambda^2}{\eta} \vec{\nabla}c = -k_B T \frac{d}{dx} \int_{-\infty}^{\infty} \frac{1}{\eta_{\pm}} y (c - c_{\pm}^s) dy \quad (2.4)$$

In equation 2.4 the x- and y-direction of the slip-velocity are expressed and the concentration values at plus and minus infinity $c_{\pm\infty}$ represent the bulk values of the corresponding fluid. Finally John Anderson states that what he calls the coefficient b , but what we from now on will call the mobility M , can vary over the particle surface so this effect has to be accounted for.

$$\vec{u} = -\langle v^s \rangle \quad (2.5)$$

As a slip-velocity is a result from the slip between two phases, the slip-velocity is relative to the fluid flow around it. Therefore can the fluid flow velocity relative to the droplet be expressed as minus the average slip-velocity. This expression was used by Moerman et al. [22] in their description of droplet enhancement below the critical Péclet number.

2.2.3 Sedimentation

One of our goals is to experimentally observe the enhancement caused by the increase in Péclet number. We have seen in figure 2.3 that below the critical Péclet number ($Pe = 4$) slow dissolution of the droplet leads to an isotropic gradient. We can also see that at higher values of the Péclet number an anisotropic gradient forms that has broken symmetry.

The idea to measure the enhancement is by a "simple" sedimentation experiment, where an external force, here gravity, acts on the droplet. This external force imposes the symmetry-breaking in the swollen micelle gradient, that leads to enhancement of the droplet's sedimentation velocity compared to its passive theoretical prediction. The asymmetric gradient pushes the droplet towards higher local surfactant concentrations. In order to predict sedimentation velocities we have to assume Stokes drag (F_d) on a spherical droplet pointing in the direction opposing the direction of motion.

$$\vec{F}_d = 6\pi\eta a \vec{u} \quad (2.6)$$

Here η is the dynamic viscosity of the surrounding fluid, a the particle radius and u the velocity of the particle. Since this formula is derived for solid particles sedimenting in a liquid, it needs to be adjusted a little as our sedimenting droplet is as well a fluid. We know for quite some years

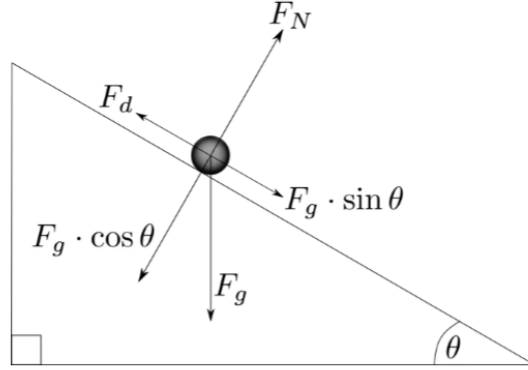


Figure 2.4: Schematic drawing of a droplet sedimenting at an inclination angle θ . Our experiments are performed at an angle of $\theta = 90^\circ$, meaning that the drag force coincides with the normal force, wherefore the $\vec{F}_d = \vec{F}_g$ equality holds.

already that sedimentation velocities depend on the Reynolds number [14]. Inman states that particles that have diameters larger than $180 \mu\text{m}$ no longer follow Stokes' law.

Even though the droplets we used are an order of magnitude smaller, the law of Stokes does not fully describes the sedimentation velocities of our droplets. The way gravity acts on a fluid particle in an surrounding liquid of different viscosity and density varies from solid particles in a sense that gravity causes a fluid flow inside the droplet itself instead of only acting on the droplet as a whole. The fluid-fluid drag coefficient was used by Michelin and Izri et al.[16, 21] and is given by:

$$C_d = 6\pi\eta_f a \cdot \frac{1 + \frac{3\eta_f}{2\eta_d}}{1 + \frac{\eta_f}{\eta_d}}. \quad (2.7)$$

Here we distinguish between the viscosity of the droplet η_d and the viscosity of the surrounding fluid η_f . The viscosity of diethyl phthalate is given by $\eta_{DEP} = 1.029 \cdot 10^{-2} \text{ Pa}\cdot\text{s}$, calculated from the empirical Williams-Landel-Ferry (WLF) equation [6] that is given by:

$$\log \eta = 1.06 - \frac{4.13T + 165}{106 + T} \quad (2.8)$$

Here T is the temperature centigrade and η is the shear viscosity in poise ($1 \text{ P} = 0.1 \text{ Pa}\cdot\text{s}$). We now have all the tools to calculate the drag coefficient, and almost all what is needed to predict the sedimentation velocities of the droplets.

The driving force for the formation of solute gradients is droplet dissolution. We measured this by tracking the droplet size in time. The dissolution below the critical Péclet number is not strong enough to self-propel particles but possibly can enhance the droplet. The one thing left is to build in an expression for the enhancement in an external field. Moerman et al. [22] stated that in case of a gravitational influence the velocity of an isotropic droplet can be written as the sum of the ratio between the external force and the drag coefficient and the mobility caused by the formed gradient.

$$\vec{u} = \frac{\vec{F}_g}{C_d} + M \vec{\nabla} c \quad (2.9)$$

Together with this gradient induced mobility $\nabla c = \frac{u(c_s - c_\infty)}{D}$ equation 2.9 can then be solved self-consistently for the particle velocity in the diffusion-limited regime of DEP swollen micelle assembly and written in terms of the Péclet number to obtain

$$\vec{u} = \frac{\vec{F}_g}{C_d} \frac{1}{1 - \frac{Pe}{Pe_{cr}}}. \quad (2.10)$$

Here the second part of the equation is the enhancement correction necessary to describe the influence of gravity (or other external forces) on the sedimentation speed of isotropic swimmers. The combination of equations 2.7 and 2.10 together with the well-known gravitational force $F_g = mg = \frac{4}{3}\pi a^3 \Delta\rho g$ leaves us with a rather large equation that we intend to provide with experimental proof.

$$\frac{\vec{u}}{a^2} = \frac{2\Delta\rho\vec{g}}{9\eta_f} \cdot \frac{1 + \frac{3\eta_f}{2\eta_d}}{1 + \frac{\eta_f}{\eta_d}} \cdot \frac{1}{1 - \frac{Pe}{Pe_{cr}}} \quad (2.11)$$

In the left part of the equation the sedimentation velocity is divided by the particle radius squared to account for experimental polydispersities. The right side of the equation exists of three parts: the external force, the correction of the Stokes drag for fluid particles and the hydrodynamic enhancement part respectively.

2.2.4 Microfluidics

In order to have control over the droplet size microfluidic devices are built via an approach as described in Appendix A. Our aim is to produce droplets that are several tens of microns in size, realised by fluid flow through tiny capillaries. These capillaries have diameters ($< 500 \mu\text{m}$) in length scales that are consistent with the low Reynolds regime, and therefore can the flow through them be described by the viscous force dominating Stokes flow.

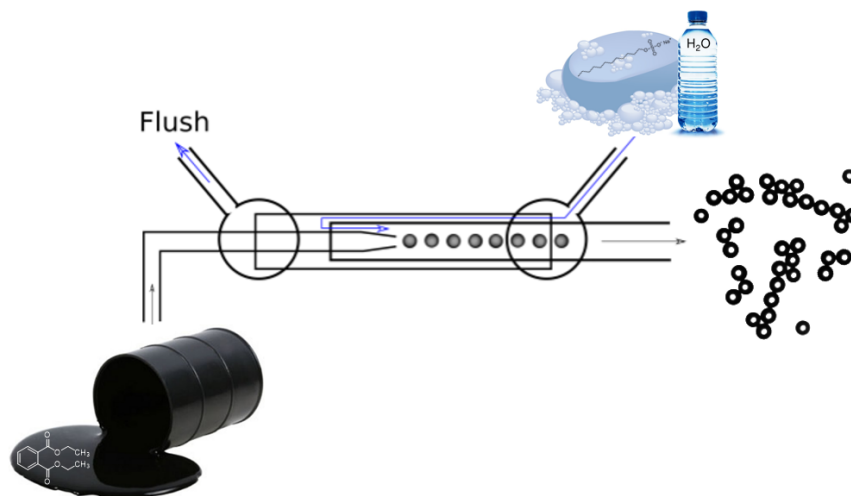


Figure 2.5: Schematic picture of a handmade microfluidic device having four inputs. Two of them are inlets denoted with in-going arrows and the two exits are shown by out-going arrows. The blue arrows represent the water containing surfactant while the grey arrows stand for the oil flow.

Larger fluid flow leads to higher shear forces on the droplet with in turn decrease the droplet size. We have worked with an constant oil flow velocity (of $100 \mu\text{m/h}$) while we varied the speed of the flow of (oil saturated) surfactant solution to obtain different sized droplets. Expressions for the laminar flow through various shaped capillaries can be found in Appendix E.

Eventually the formed droplets are dispersed in oil saturated detergent-water, where they are immediately stabilised by surfactant molecules that are present in the solution. Since the droplets will be dispersed the oil flow is called the dispersed phase. The same way of thinking goes for the continuously flowing surfactant solution, this is called the continuous phase. The fluid flows through the channels are induced by an experimental syringe setup.

2.2.5 Particle tracking

Circular Hough transform

A very powerful tool to quickly process image data obtained using (light) microscopy is particle tracking. A stack of images is provided and a tracking algorithm (provided in Appendix B) goes through all the images one by one and outputs a list of coordinates of all particles found in each frame. The idea itself is fairly simple and straight forward, the way to get there can be rather complicated, as image resolution, focus of the to-be-found particle and the chosen algorithm parameter greatly influence the outcome.

Paul Hough patented in 1962 [12] a way to computationally track lines and complex patterns, an approach that is further developed to be able to track all kinds of shapes. The detection method used in this research is called the Circle Hough Transform (CHT) and for this method to be able to detect spherical objects we roughly need to know the size of the particle (in pixels). The boundary conditions inputted in this tracking algorithm are the particle radius so the code has some frame of reference in what range it should search. In this range the script looks for strong contrast difference peaks which each of them will be taken as a circle centre (a, b) expressed as 2.12 in parameter space of radius r provided as input by the user.

$$\begin{aligned} x &= a + r \cos \theta \\ y &= b + r \sin \theta \end{aligned} \tag{2.12}$$

If multiple of those peaks are found that fall on the perimeter of the to-be-detected particle, circles of the provided radius are drawn around them in parameter space. The circles around these tracked points will intersect at the exact centre (x, y) of the to-be-tracked sphere, as is shown in figure 2.6. This approach leaves some space for iterating to the exact radius of the sphere as adjusting the radius will either converge or diverge from the intersect.

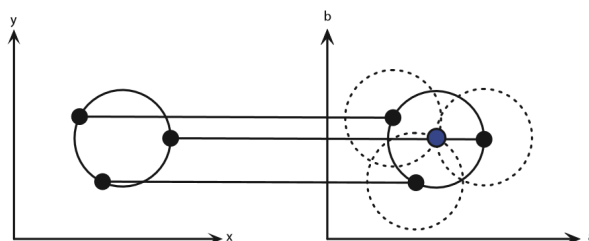


Figure 2.6: On the left hand side we see the found contrast peaks in the image, with in the left parameter space dashed circles drawn around them that intersect in the middle of the circle. Image taken from Simon Pedersen [28].

Track combination

Once tracking is done and coordinates are listed for all frames, the challenging part is connecting the individually found particles into tracks. The complexity of this problem will be illustrated by means of figure 2.7. We have a set of consecutive frames all tracking multiple particles. The computer cannot follow the path of the particles as a person would do while watching the video, so a clever way is needed in order to connect particle positions into tracks. In 1996 John Crocker and David Grier provided the scientific community with a method to do the trick [7], an algorithm that nowadays is improved (and in some places slightly changed) by Daniel Blair and Eric Dufresne from the Universities of Georgetown and Yale respectively [4], other algorithms by different authors are present but essentially provide us with the same result.

The code works with a couple of predefined parameters that can be tuned accordingly to the users needs, and need to be dealt with properly as results are highly dependent on those

parameters. The most influential parameters are the maximum displacement, the dimensionality and the minimum length a trajectory needs to have to be addressed as an actual particle. When we look at figure 2.7 it is not immediately clear where the particle in *frame i* ends up in *frame i+1*. We distinguish between the positions and coupling the correct position to the right track by setting a value for the maximum displacement.

Let us consider a particle A and particle B as is illustrated in figure 2.7, it is assumed that of the different permutations available, the travelled distance is always smaller than the value set by the maximum displacement. That means, when comparing two consecutive frames, i and $i+1$, it is assumed that a particle can never travel a distance (at $i+1$) further than initially set by the maximum displacement, therefore in this illustration its actual displacement is the shortest distance from its initial position (at i). Thus the particle at the top left corner (in *frame i*) travels to the bottom left corner (in *frame i+1*), as this is the shortest distance from its original position. Note that this trick only works when particles are further apart than the maximum displacement.

Here the dimensionality is always 2, since the microscopic images obtained are two dimensional and the minimum length is set to 10, meaning that if a particle is found in less then 10 consecutive frames the found track is thrown out. If all those parameters are set well and the code does its work, we end up with a list containing all droplet positions and radii in numbered frames, where individual particles are labelled with a number.

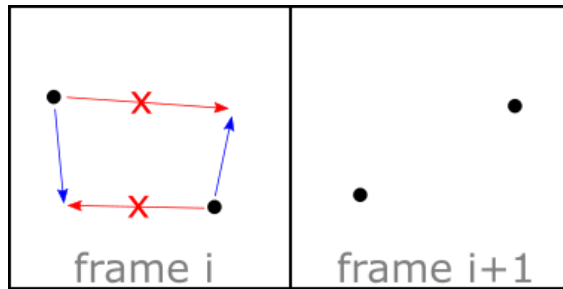


Figure 2.7: Illustrative depiction of the difficulty to connect tracking coordinates. Based on this image it is hard to tell if the upper left particle (in frame i) moved to the right or swam to the bottom.

2.3 Materials and methods

2.3.1 Surfactant (stock) solution preparation

1L of a 100 mM sodium dodecyl sulfate ($\text{NaC}_{12}\text{H}_{25}\text{SO}_4$) stock solution was prepared by dissolving 28.84 g SDS (BDH, $M_w = 288.372$ g/mol, 99%, CAS: 151-21-3) into 1L of MilliQ under vigorous stirring.

The diethyl phthalate (Alfa Aesar, $M_w = 222.24$ g/mol, 99%, CAS: 84-66-2) saturated water was prepared by bringing 100 μL $\text{C}_{12}\text{H}_{14}\text{O}_4$ (solubility in water 1080 mg/L at 25°C) into a 50 mL MilliQ. This solution was centrifuged and the DEP saturated water was carefully brought into a glass vial and was labeled as 0 mM SDS.

The 2 mM SDS surfactant solution was made by addition of 0.4 mL stock solution into a glass vial and filling it up to 20 mL with 19.6 mL MilliQ.

The 4 mM SDS solution was made by filling 0.8 mL stock solution up with 19.2 mL MilliQ.

20 mL of 5 mM SDS solution was prepared by filling 1.0 mL of stock solution up with 19 mL MilliQ.

The 6 mM SDS solution was prepared by filling 1.2 mL stock solution up with 18.8 mL MilliQ.

The 7 mM SDS solution was made by addition of 18.6 mL MilliQ to 1.4 mL 100 mM SDS stock solution.

2.3.2 Microfluidics

The pressure of the continuous flow, a DEP saturated 10 mM SDS solution, is set to 5 psi (pound-force per square inch) using a pressure gauge driven by compressed air, and the dispersed flow (DEP) is set to 100 $\mu\text{L}/\text{h}$. We waited until the flow in the device relaxed and collected the droplets (dispersed in the DEP saturated solution) over a period of 1 hour in a small glass vial. Droplets of about 12 μm in size were obtained, that appeared to be quite stable in the DEP saturated solution, and were kept inside the small glass vial.

2.3.3 Sedimentation experiments

Individual sedimenting droplets are required to obtain reliable data in which surrounding flow patterns are not influenced by flow profiles induced by neighbouring droplets. Therefore dilution of the sample obtained from microfluidics is recommended in order to reduce the amount of collected droplets that will be used for sedimentation.

The gravitational experiments performed in this research have been visualised using a Nikon Eclipse LV100 tilted microscope with an 10x/0.3 DIC L lens and have been recorded by a DMK 23UX174 camera from The Imaging Source at a frame rate of 25 frames per second, calibrated to 1.6680 pixel/micrometer. The 0 mM SDS solution is saturated with DEP as a control to avoid droplet shrinkage.

Since the droplets are dispersed in a different solution than in which the experiments is performed, we first diluted the droplets in the right solution and then added them to the experimental setup. This way we avoided mixing of the DEP saturated solution with the unsaturated aqueous SDS solution in the experimental setup. Avoiding mixing is required as in an earlier stage it was observed that the pipetted quantities sediment as a whole. This observation means that the droplets keep being emulsified in the DEP saturated solution and therefore cannot dissolve as a result of swollen micelle formation, since they remain in a DEP saturated environment. The procedure below is followed for the enhanced regime, but in this regime rapid working is not a necessity.

For higher surfactant concentrations than 4 mM some rapid work is required in order to prevent the droplets from shrinking too much upon dilution using the matching surfactant solution. Therefore the 10 μL of DEP saturated 10 mM SDS solution containing the droplets were pipetted into a 200 μL of the corresponding surfactant concentration solution, mixed and 10 μL was taken and pipetted into the sample well (from which fabrication can be found in appendix C).

2.3.4 Characterisation

Characterisation was done using particle tracking, from which we could obtain the sedimentation velocities in micrometer per second by multiplying by the frame rate and division through the microscope calibration.

2.4 Results and discussion

2.4.1 Passive and enhanced sedimentation

Since we are able to produce (a narrow distribution of almost) equally sized droplets, sedimentation experiments were done by diluting and pipetting small amounts into our sample well. Since shearing and mixing can lead to the coagulation of (initially monodisperse) droplets and dilution of the saturated solution with unsaturated SDS solution leads to dissolution and thus shrinkage, some polydispersities cannot be prevented. For that reason we had to take possible polydispersities into account. To correct for differences in droplet sizes our measured velocities were divided by the droplet radius squared (\vec{u}/a^2), as was formulated in equation 2.11.



Figure 2.8: Snapshot of two comparable sized droplets ($\sim 10 \mu\text{m}$) sedimenting in the same time-frame at different surfactant concentrations. The droplet on the left is moving passively, whereas the right droplet is enhanced by its solute gradient.

In figure 2.8 this is illustrated by plotting the particle trajectory (of similarly sized droplets) on top of the last frame. The experiments were recorded over the same amount of time, and the droplet sedimenting at 7 mM SDS clearly sedimented faster.

2.4.2 Droplet shrinking

In figure 2.9 the typical size decrease in time is shown for two typical droplets, here the slope acquired from linear regression analysis indicates the shrinking rate, whereas the intercept provides us with the initial droplet size. It clearly shows that the size determination from particle tracking is noisy, so for reliable shrinking rates sufficiently long trajectories (or high frame rates) of well-focused droplets are required.

The shrinking rates plotted in figure 2.10 are experimentally obtained using particle tracking, by plotting the droplet diameter obtained from all consecutive frames, scaled to the frame rate of 25 frames per second. Note that the most left red point has as negative shrinking rate, meaning that the droplet is growing. The experiments at 0 mM SDS have been performed in a DEP saturated solution to prevent shrinking, and droplet growth in this case is merely an effect of particle tracking that can slightly deviate in size determination as a result of the microscope focus of the droplet upon recording.

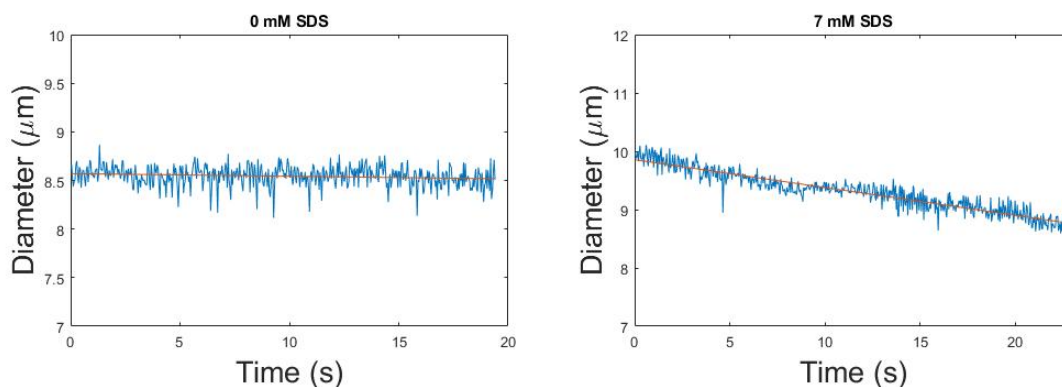


Figure 2.9: The shrinkage of the droplet size as function of time for two different surfactant concentrations showing that droplet dissolution takes place above a certain threshold surfactant concentration (~ 4 mM SDS, $Pe = 0$).

When taking a closer look at the shrink rates in figure 2.10 and look beyond the noise, it is observed that (for reasonably monodisperse droplets) the rate of shrinking increases with the surfactant concentration. A result that also is observed in the size declines and seems straight forward as more fuel results in faster recoverage of surfactants at the oil-water interface and thus in faster expulsion of oily micelles. At sufficiently high surfactant concentrations (6-7 mM SDS) the rate of shrinking is that high that droplet enhancement is observed.

The shrinking rate is related to the surface tension since the droplet solubilisation into the micellar solution occurs via a slip-velocity that inhomogenises the surfactant concentration on the surface, and in order to self-sustain the surface tension, the interfacial tension gradient is counteracted by a Marangoni flow. As surface tension as well as solubility are functions of temperature, the dissolution rates vary as temperature fluctuates from day to day.

2.4.3 Experiments compared to predictions

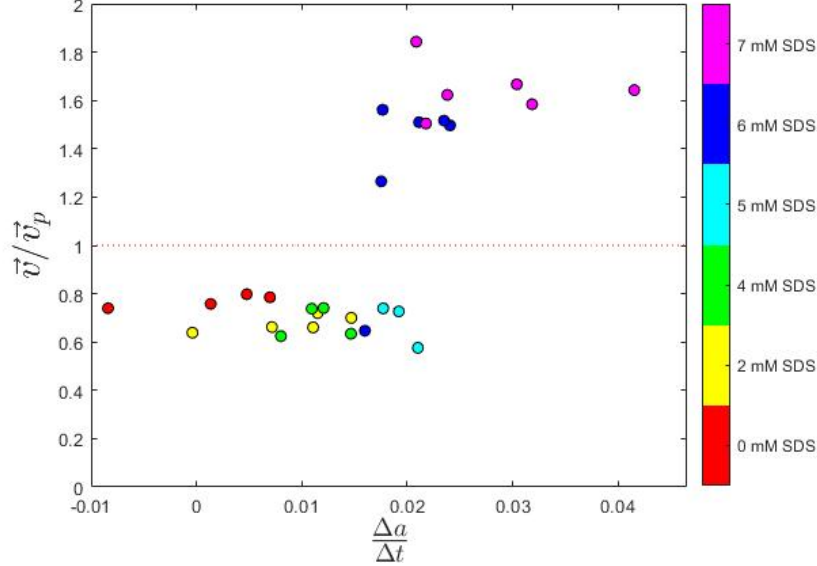


Figure 2.10: Sedimentation velocities scaled to their predicted values of monodisperse droplets versus their rates of shrinking. The dashed line at $\vec{v}/\vec{v}_p = 1$ symbolises the value where the experimentally obtained velocity equals the theoretical prediction, and therefore serves as a partition line between the passive and enhanced sedimentation velocities.

In figure 2.10 the experimentally obtained sedimentation velocities are scaled to the predicted velocity based on the Stokes drag and density of the particle (the passive form of equation 2.11), and plotted versus their shrink rate. The dashed line at $\vec{v}/\vec{v}_p = 1$ serves as the distinction between the passive regime where sedimentation velocities approximately behave as predicted (below $\vec{v}/\vec{v}_p = 1$), and the enhanced region where sedimentation velocities are enhanced by their solute gradient and sediment faster than would be predicted by classical sedimentation theory (above $\vec{v}/\vec{v}_p = 1$).

In table 2.1 the numerical data is shown that lay on the basis of figures 2.10 and 2.11. From these data values we cannot see the expected trend that an increase in droplet size leads to a decrease of the shrinking rate. Even though the shrinking rates roughly agree with the data presented in figure 2.2 we have to conclude that particle tracking only provides us with a rough measure for the rate of shrinking. Note that the shrinking rate values presented in the table are values of the shrinking of droplet radius.

Table 2.1: Numerical data (as retrieved from MATLAB) of the droplets related to figure 2.10 and 2.11 as recorded at 25 frames per second. Sizes are averaged over all obtained sizes by particle tracking and the predicted velocity is based on the average size, whereas the experimentally obtained velocities are based on time difference between the first and last frame.

\bar{v} ($\mu\text{m/s}$)	\bar{v}_p ($\mu\text{m/s}$)	\bar{v}/\bar{v}_p	$\Delta a/\Delta t$ ($\mu\text{m/s}$)	$2a$ (μm)	# frames	c (mM SDS)
4.0071	5.2878	0.7578	0.0014	8.5702	485	0
6.0506	7.7074	0.7850	0.0070	10.3879	260	0
6.1902	8.3670	0.7398	-0.0084	10.6867	180	0
7.9727	9.9924	0.7979	0.0048	11.7739	150	0
6.7428	9.6330	0.7000	0.0147	12.0145	820	2
10.4965	15.8926	0.6605	0.0111	15.0486	533	2
11.4196	17.2544	0.6618	0.0072	15.5801	510	2
14.5759	20.2464	0.7199	0.0115	16.9014	397	2
17.4582	27.3392	0.6386	-0.0004	19.4223	326	2
11.2270	15.2165	0.7378	0.0109	14.7155	506	4
11.0901	17.7597	0.6245	0.0080	15.8242	517	4
12.9514	20.4158	0.6344	0.0147	17.0498	445	4
19.7206	26.6280	0.7406	0.0121	19.3110	285	4
19.0695	26.2372	0.7268	0.0192	19.2568	292	5
20.5731	35.7170	0.5760	0.0210	22.4323	269	5
30.5906	41.3862	0.7391	0.0177	24.0006	137	5
17.5198	11.6031	1.5099	0.0211	12.9199	311	6
8.6023	13.3007	0.6468	0.0160	13.8787	512	6
22.5919	14.4695	1.5613	0.0177	14.3066	244	6
20.5365	16.2334	1.2651	0.0175	15.1300	227	6
25.0194	16.5001	1.5163	0.0235	15.3097	230	6
30.2093	20.1846	1.4967	0.0241	16.8661	179	6
10.1876	6.2774	1.6229	0.0238	9.8549	572	7
15.8268	8.5874	1.8430	0.0209	11.1158	272	7
16.3438	10.8646	1.5043	0.0218	12.4996	289	7
28.1675	17.7815	1.5841	0.0319	15.9161	194	7
32.1024	19.5436	1.6426	0.0416	16.7098	170	7
37.8670	22.7210	1.6666	0.0304	17.8833	141	7

2.4.4 Sedimentation results

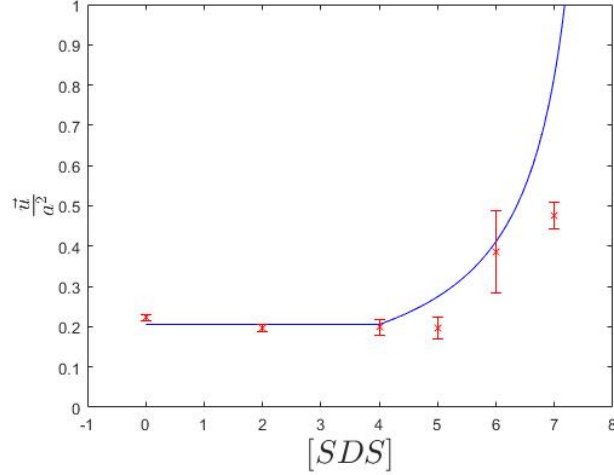


Figure 2.11: Experimentally observed sedimentation data at different surfactant concentrations plotted on the theoretically predicted equation 2.11 taking a threshold value of $Pe_{cr} = 4$.

Figure 2.11 shows the experimentally observed averaged \bar{u}/a^2 data for each surfactant concentration, where the droplet size is taken to the mean value of the values obtained from particle tracking. The plotted fit is the theoretical prediction by Moerman et al. [22], note here that the theoretical prediction is shifted down by multiplying the equation by a prefactor $pf = 0.7102$. The prefactor is given by the mean value of the passive droplets ($[SDS] = 0, 2, 4$ mM) divided by the theoretical prediction at this passive regime. Three distinct regimes can be characterised: as just mentioned, from 0 to 4 mM SDS droplets behave passively and therefore the line is constant at these values. Above 4 mM dissolution takes place but until 8 mM, in this regime no self-propulsion but enhancement of the sedimentation velocity occurs. Above 8 mM of the surfactant self-propulsion occurs and we will deal with this regime in the next chapter.

When looking at figure 2.11 it is clear that the experimental results do not plainly fit the physical equation 2.11, but that above the value of $Pe = 1$ there is enhancement of the velocity as a result of dissolution. At $Pe = 1$ the time scales of dissolution and diffusion are equal, meaning that there is isotropic dissolution that should be able to enhance an external force. We chose to plot our laboratory results according to the theoretical value imposed by Michelin et al. (i.e. $Pe_{cr} = 4$), whereas it seems plausible that the comparison $Pe \approx [SDS] - 4$ not merely holds. The assumption made is that $Pe = 0$ coincides with the with CsMC, and that the critical Péclet coincides with the CMC and therefore is dependent on the temperature.

Perhaps the environmental conditions were not ideal during the experiments, and therefore it might be that the critical Péclet number turned out to lay higher (meaning that enhancement occurs at a higher surfactant concentration). Note that the function represented by the blue line goes to infinity at the critical Péclet number, in practice this value will go to the swimming velocity upon self-propulsion meaning that its \bar{u}/a^2 value will lay lower.

Overall we can conclude that the approach of [22] is roughly right and that figure 2.11 shows that solute gradients resulting from droplet dissolution can influence the sedimentation velocities when swollen micelle formation is abundant.

2.5 Conclusions

We have investigated the effect of solute gradients on their sedimentation velocities, and from our data the conclusion can be drawn that solute gradients (below the critical Péclet number) are able to enhance the sedimentation velocities of our isotropic droplets.

Particle tracking proved to be a good tool for qualitative sedimentation studies, but as the size determination is not exact, the determination of properties related to the size is neither. However the obtained rates of shrinking seem to be in agreement with earlier published results, as can be concluded that higher surfactant concentrations lead to faster shrinking rates.

Microfluidics allow us to selectively produce droplets that are in the tens of micrometer size range depending on the size of the capillaries that are used for the construction of the device. The droplets obtained from microfluidics are fairly monodisperse and can be used for sedimentation experiments. Polydisperse samples lead to some noise in the data, but can be used as the formulation of the sedimentation velocity (\bar{u}/a^2) is taken into account.

Chapter 3

Self-propulsion above the critical Péclet number

3.1 Introduction

The swimming direction of self-propelling droplets is not predetermined by their surface properties. In chapter 2 we have seen that DEP droplets dissolve in a sufficiently high concentrated surfactant solution (above the CsMC), and it was stated that above a critical Péclet number self-propulsion will occur. In chapter 1 we saw that Izri et al. managed to create self-propelling water droplets in oil. These isotropic swimmers are fundamentally different from Janus particles as Janus particles have a partly coated surface and therefore its swimming direction is predetermined.

For isotropic droplets the dissolution occurs isotropically, meaning that its swimming direction is unknown and depends on the local surfactant concentration, since the tendency to recover a homogeneously covered surfactant layer at the droplet surface makes the droplet swim to regions where the surfactant concentration is locally higher. This implies that the motion of a droplet is not intrinsically defined by the droplet itself, but is a reaction to the events happening in the environment and thus related to the surrounding flow field.

It is a given fact that particles are affected by nearby fluid flow. Tiny droplets are also influenced by surrounding flow that can lead to a change in the direction of such moving droplets. This concurrently means that the solute trace these droplets leave behind, have the potential to interfere with (the gradient of) neighbouring droplets.

First we will study droplet trajectories by looking at the progression of the pathways of these droplets in time. Various sized droplets will be studied, as the critical size mentioned by Michelin et al. [21] raised the presumption that multiple swimming regimes exist in which droplets might behave differently.

As an additional method to study the movement of these droplets, we will have a closer look at the fluid flow around them by experimentally tracing the fluid flow. The method employed for this purpose is called particle image velocimetry (PIV) and allows for observation of the fluid flows, represented in our case as two-dimensional vector fields.

In this chapter we will examine what type of movement our isotropic DEP droplets have as a result of their dissolution, which will be done according to several analysis techniques related to the trajectory of the droplet, and relate their motion to the surrounding fluid flow. The question we will attempt to answer here, is what type of motion determines the movement of droplets and how this is related to the fluid flow around them. The different regimes will be probed using microfluidics, to have control over the droplet size.

3.2 Theoretical background

3.2.1 Mean square displacement

In order to obtain information about how the droplet's swimming direction changes we will use three approaches. The **first** way of extracting information from particle trajectories is by means of the mean square displacement (MSD). The MSD relates particle positions separated by a fixed time step Δt , lists them and takes an average. This is subsequently done upon increasing Δt steps, and is defined in equation 3.1. In this expression x (and $x_n(t)$) stands for a position a time step Δt away from the reference position x_0 (and $x_n(0)$). Here N stands for the number of time steps that depends on the magnitude of Δt .

$$\text{MSD} \equiv \langle (x - x_0)^2 \rangle = \frac{1}{N} \sum_{n=1}^N (x_n(t) - x_n(0))^2. \quad (3.1)$$

Back in May 1905, Albert Einstein approached the motion of passive suspended particles from the point of thermodynamics and described their movement as a random walk [9]. He found that in order to specify the motion of a randomly diffusing particle the displacement does not grow linear in time but is on average zero. Therefore it is more useful to follow the quadratic displacement in time, as this mean square displacement does (for randomly moving Brownian particles) evolve linear in time.

The conclusion that can be drawn from this, is that the slope of the MSD in a log-log plot will determine with what type of motion the droplet moves. A slope of zero tells that the droplet does not move and is confined in space. For a slope of one the particle movement originates from the fluid that flows around it, and therefore is diffusive random motion from which the MSD scales linear in time. For a slope value of two, the displacement grows linear in time (and on average does not equal zero), meaning that a particle moving a time t with a certain velocity \vec{u} has a displacement of $\vec{s} = \vec{u}t$. This type of motion is called ballistic motion from which the MSD grows quadratically in time.

Einstein stated: "die Wurzel aus dem arithmetischen Mittel der Quadrate der Verrückungen in Richtung der X-Achse; es ist: $\sqrt{x^2} = \sqrt{2Dt}$." In Einstein's form we can clearly see that the square of the displacement grows is linearly related to time. The diffusive expression for the MSD that generally applies to more than a single dimension is given by:

$$\langle r^2 \rangle = 2dDt \quad (3.2)$$

in which d is the dimensionality, $D = \frac{k_B T}{6\pi\eta_f a}$ the Stokes-Einstein diffusion coefficient and time t . Here is equated that the quadratic displacement grows linear with time. Howse et al. [13] relates the two-dimensional form of Einstein's expression of the Brownian MSD to ballistic motion and equates it as:

$$\langle r^2 \rangle = 4Dt + \frac{\vec{u}^2}{2D_r^2} [2D_r t + e^{-2D_r t} - 1]. \quad (3.3)$$

In this equation $D_r = \tau_r^{-1} = \frac{k_B T}{8\pi\eta_f a^3}$ is the rotational diffusion coefficient that equals the reciprocal rotational diffusion time scale. Now two limits can be distinguished: At short times $t \ll \tau_r$ the mean square displacement is dominated by ballistic steps and given by $\langle r^2 \rangle = 4Dt + \vec{u}^2 t^2$, whereas at longer times $t \gg \tau_r$ the limit is dominated by the rotational diffusion and given by $\langle r^2 \rangle = (4D + \vec{u}^2 \tau_r) t$.

3.2.2 Velocity autocorrelation function

The **second** approach is the velocity correlation function (VCF). This orientational autocorrelation function is a statistical function somewhat similar to the mean square displacement method. Where the MSD provides information about translational motion, from which in specific cases a

translational diffusion coefficient can be obtained, the VCF feeds us with knowledge about the orientation of a particle, with respect to its initial direction, after a certain moment in time.

$$C(\delta t) = \langle u(t) \cdot \hat{e}(t) \rangle = \frac{1}{N} \sum_{i=1}^N u_i(t) \cdot \hat{e}_i(t) = e^{-t/\tau_r} \quad (3.4)$$

To elaborate: it is a timewise measure during which the orientations of these self-propelling droplets are correlated. Therefore the VCF provides us with rotational information from which we can extract a rotational diffusion coefficient [34, 41]. Here u_i is the velocity vector at time t and \hat{e}_i the unit vector accounting for the initial intrinsic direction, τ_r is called the *orientational correlation time* or the *persistence time* and is in the case of Janus particles equally related to the rotational diffusion coefficient as was mentioned in the previous section. Later we will examine if this relation also holds for isotropic droplets.

3.2.3 Rotation angles

The **third** approach of quantifying the motile behavior of the various sized droplets is by rotation angles. Here we extract their intrinsic direction from the coordinate trajectories obtained from particle tracking. For expressing this direction we have to take a look at three following positions to

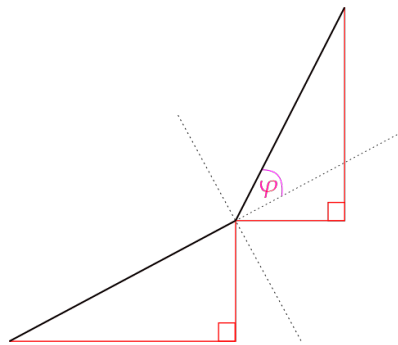


Figure 3.1: Three droplet positions schematically depicted at the black line corners, the red horizontal and vertical lines respectively represent Δx and Δy between the two consecutive positions, the connecting solid black hypotenuse stands for the velocity vector between the two points, whereas the dashed black line extends the initial droplet direction. Here the in purple φ is the rotation angle with respect to the initial droplet direction.

be able to obtain the deviating angle with respect to its initial direction. Particle tracking provides us with a list of x- and y-positions of the droplet in each frame, based on those coordinates we can calculate the differences in x- and y-positions between two sequential frames and get the angle with respect to the x-axis as:

$$\alpha_i = \arctan \frac{\Delta y}{\Delta x} = \arctan \frac{y_{i+1} - y_i}{x_{i+1} - x_i}. \quad (3.5)$$

Now the rotation angle φ we are looking for, visualised in purple in figure 3.1, is merely the difference of two subsequent angles α . By convention negative angles belong to counter-clockwise rotation, so turning left and all positive angles account for clockwise rotation. For this reason we express our rotation angle as:

$$\varphi_i = \alpha_i - \alpha_{i+1}. \quad (3.6)$$

A disadvantage of particle tracking is that the tracking precision is on the order of one pixel. At high frame rates, when the displacements are small, this leads to large rotation angles that are not real but an artifact of the finite tracking precision. Smoothing up the tracks by using a

moving average filter works very well in removing rotational noise from the tracked data and was used for the straight trajectories.

When, according to the tracks, it seems like the droplet is moving backwards subtracting angles becomes more complicated. Whenever an angle exceeds $\pm \pi$, this needs to be corrected by adding up opposite signed $\pm 2\pi$ to really obtain the angle that we are interested in. We will later show that this approach leads to rotation angles that are consistent with our observations.

3.2.4 Particle image velocimetry

Since we do not only want to analyse the droplet trajectories but also test the flow around these droplets, we need to visualise the fluid flow. In order to practically visualise the flow inert [25] tracer particles are necessary. These $1 \mu\text{m}$ sized polystyrene (PS) tracer particles don't interfere with the flow stream but do give us a clear view on how the flow proceeds. These tracers are carried by the flow that is induced by perturbations, or more importantly created by the flow field around the drop as a result of the interplay between gradient formation and diffusion.

Since the PS tracers do not affect the flow they can visualise what is happening in close proximity around the droplet of interest. Videos were recorded observing dispersed swimming droplets in surfactant solution containing tracer particles such that the flows are clearly visualised. The videos were recorded using an optical microscope at a frame rate of 100 frames per second and cut into a series of frames.

Thielicke et al. [35] provides us with a tool to analyse the images quantitatively: PIVlab. PIV stands for Particle Image Velocimetry and PIVlab is a tool in MATLAB to visualise flow fields. The way PIVlab analyses our image stacks is by dividing each frame in different sized squares and analyse them based on their mesh size. PIVlab can handle different mesh sizes and the meshes will be individually compared to the corresponding mesh in the subsequent frame.

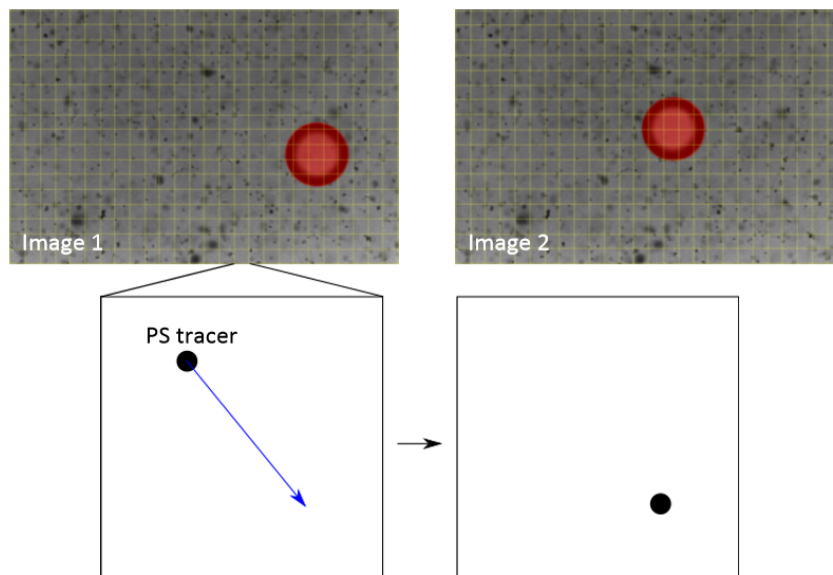


Figure 3.2: Schematic representation of the Particle Image Velocimetry idea.

At first PIV will compare two consecutive large meshes in order to find patterns like vortices, and continues to go through all squares going from large to small meshes. In the smallest mesh sequential squares are compared and checked for differences in contrast peaks, so when tracer particles have moved between frames this is noticed and the movement is represented as a vector, as can be seen in figure 3.2.

Each small square represents a vector and the combination of all vectors with the (statistical) patterns obtained from larger meshes makes up the most reasonable overall flow field. So after the

calculations PIVlab provides us with a new stack of flow fields (one less than the initial recorded stack) that are all obtained by comparing two consecutive images.

3.2.5 Types of fluid flow fields

The literature provides us with fluid flow fields that we expect to see. Among others, Anderson (1989) [3] as well as Zöttle and Stark (2016) [41] published typical velocity fields for phenomena like sedimentation and osmophoresis. In figure 3.3 the results from Zöttle et al. are shown, and are the typical flow fields that can be observed around spherical particles. In the left image a flow field is shown that is driven by some external force, a typical flow field for a single point force in a fluid and therefore is called a stokeslet (a force acting on a point in a Stokes flow).

The middle image appears to be a quadrupole but is what in the literature is referred to as a force dipole. A force dipole results from having two point forces that act in opposite directions, and even though two planes of symmetry can be drawn it are those two forces that make the resulting flow field a (force) dipole. The image on the right clearly is a dipole and is called a source dipole, here we consider what is called a source and a sink. Two joined points; from the source all stream lines point outward, whereas in the sink all stream lines come together pointing inwards.

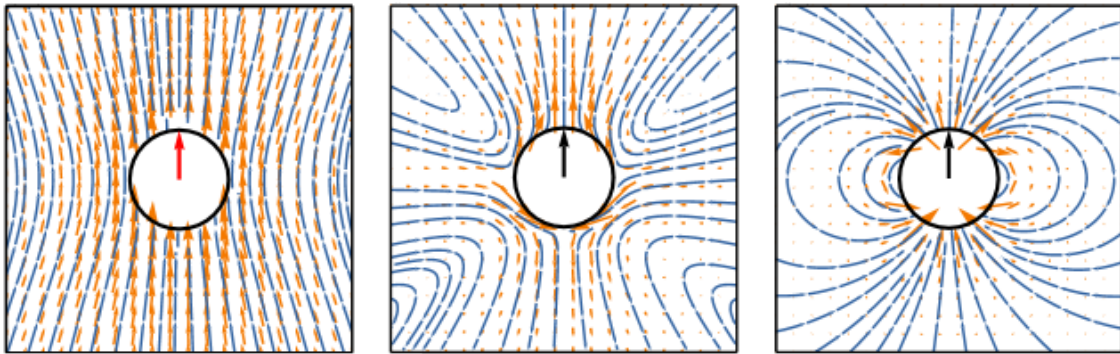


Figure 3.3: Flow fields around spherical droplets, where the orange arrows denote the velocity fields and the blue coloured represent the stream lines. In the left image a typical flow field driven by an external force (red arrow) like gravity is shown. The middle image shows a force dipole and in the right image a source dipole are presented where the black arrows indicate swimming velocities. Images taken from Andreas Zöttle and Holger Stark [41].

When an droplet swims in an incompressible liquid, without it being guided by an external force, it pushes fluid away in the moving direction, that needs to be filled up at the rear end. So when a 2D slice through the centre of a passive spherical particle is taken parallel to the swimming direction, one would expect to see a (source) dipolar flow field. Our study will be performed using light microscopy, and since optical microscopy is a two-dimensional technique similar flow fields are expected. However, be aware that fluid flows are three-dimensional phenomena, as is schematically depicted in figure 3.4.

Drescher et al. [8] have done experimental tests on swimming *Escherichia coli* bacteria and concluded that the pusher force dipole is in good approximation with the measured flow field surrounding *E. coli*. Also was found that the hydrodynamic effects, ranging in the same order of magnitude as the droplet's diameter, are dominated by rotational diffusion. Drescher states that: "Larger organisms may display even stronger rotational diffusion due to enhanced intrinsic swimming stochasticity." [8, 30] A force dipole does not have a well-defined direction and therefore is randomly contributing to its overall orientation, meaning that this type of flow field does not contribute to the droplet's propulsion.

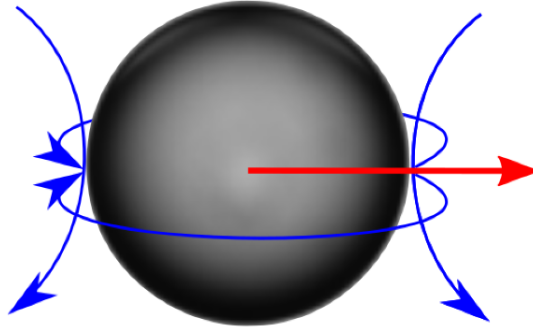


Figure 3.4: Illustrative presentation of the flow around a autophoretic isotropic droplet, a three-dimensional phenomena in which the surfactant supply comes from above and the observed fluid fields lay in the horizontal plane of the droplet.

3.2.6 Velocity decays

The observed flow fields can be quantified by looking at their velocity decay. Predictions for these decays have been done in the literature [3, 18, 41] stating the decays of the flow fields shown in figure 3.3. In an ideal situation where there are no perturbations in the flow, the flow around a moving (self-propelling) particle will slowly decay to a steady bulk velocity that as a result from random thermal molecular movement would on average be zero.

In our computational description of the flow fields we make use of a set of four matrices; the x- and y-matrix stating all x- and y-positions respectively, and an u- and v-matrix in which all x- and y-components of the flow velocity are saved. Upon averaging the flow fields are rotated such that their directions point towards the positive x-axis. To obtain the radial decay in the tangential direction, from now on described as the tangential decay, only the values from the v-matrix are taken into account. Here we only consider the values of the v-matrix that are in the vertical line perpendicular to the moving direction taken from the centre of the droplet.

John Anderson mentions that upon sedimentation the decay of the velocity field is inversely proportional to its radius r^{-1} [3]. Spagnolie et al. state that a force dipole decays inversely proportional to the radius squared r^{-2} and a source dipole inversely proportional to the radius cubed r^{-3} [33]. The obtained flow profiles should provide us with this information, where the decay of the fluid velocity has to be taken tangential (so perpendicular) to the swimming direction.

The magnitude of the fluid flow velocity can be obtained by the radial velocity decay (as a function of particle size), this can easily be calculated as the velocity vector at each point taken a radial distance away from the droplet its centre-of-mass. From the radial decay we can also determine at what distance from the droplet centre the majority of the fluid velocity has decayed to the steady bulk velocity, a feature that we will use in the next section.

3.2.7 Symmetry number

In an attempt to relate the droplet trajectories to their surrounding flow profiles, we introduce the concept symmetry number. It seems plausible that when a droplet makes a turn, this will affect its local flow profile at that moment in time, and therefore information about the travelled path is expected to be hidden in the (average) flow profile. If we consider a swimmer that moves in a perfectly straight line, the resulting flow field would be expected to be a perfectly symmetrical (source) dipole.

In that case there is a symmetry line intersecting the droplet centre parallel to its swimming direction, as is depicted in the middle image in figure 3.5. Assuming this cross-sectional line of symmetry we can look for imperfections in the symmetry, by cancelling out the x- and y-directions of the flow velocity between two interlinked points on both sides of the symmetry line, indicated

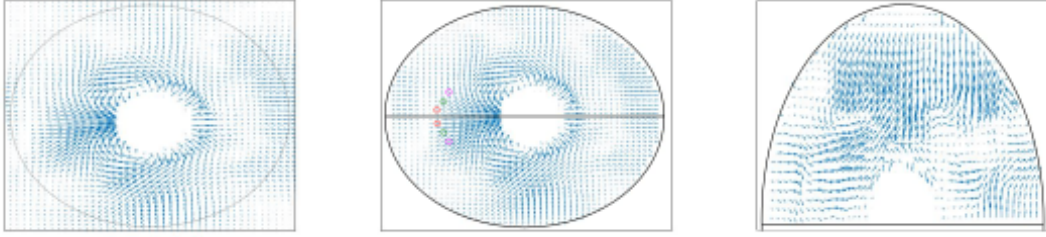


Figure 3.5: Illustrative pipeline for the symmetry analysis, with a cutoff radius of $4a$ for clarity. From left to right: the full calculated average, the circular shaped average including the line of symmetry and the semicircular resulting flow symmetry matrix.

by coloured circles in the same image of figure 3.5. Taken u to be the x-component of the velocity and v to be the y-component, the symmetry number would mathematically be described as:

$$\sigma_S = \sum_{i=1}^m \sum_{j=1}^{n/2} (u_{i,j} - u_{i,n-(j-1)}) + (v_{i,j} + v_{i,n-(j-1)}). \quad (3.7)$$

From the radial velocity decay a cutoff radius will be determined based on the distance from the droplet centre where the fluid velocity has decayed to about 10% of its initial magnitude. This cutoff is used in our symmetry analysis, and will function as a circular boundary outside which the resulting flow velocities are considered random and not contributing to the flow profile induced by the swimming droplet. Since the symmetry number analysis is done on average flow profiles, those are for reasonable results restricted to some criteria.

1. Droplets cannot be closer than ± 2 diameters to the wall, this to make sure that the obtained flow profile is averaged over approximately equally distributed flow from all sides.
2. Droplets cannot move too much in the third dimension, as fluctuations in the droplet focus leads to biases of the flow fields since (monopolar) flow from the third dimension will interfere with the flow in the horizontal plane.
3. The calculated average needs to be averaged over a sufficient amount (at least 100) of frames in order for the average to be considered reliable.

Since we hope to find correlations in the fluid flow with respect to their trajectories, this experiment is repeated for droplets of increasing size.

3.3 Materials and methods

3.3.1 Surfactant solution preparation

20 mL of 10 mM SDS containing 40 μL 4.2 wt% 1 μm polystyrene was prepared by bringing 2 mL of stock solution (preparation described in Chapter 2) into a glass vial and mixed together with 40 μL PS tracers (the ideal ratio according to [25]) and fill it up to 20 mL by adding 17.96 mL MilliQ.

The DEP saturated 50 mL 10 mM SDS continuous phase used in microfluidics was prepared by bringing 5 mL 100 mM stock solution and 0.5 mL DEP together and fill it up to 50 mL by addition of 44.5 mL MilliQ. The solution was oversaturated and the tracer of oil were removed after centrifugation.

3.3.2 Microfluidics

The initial approach of droplet formation by mixing oil, water and soap together and shaking the mixture leads to a highly polydisperse sample. As size control was required, microfluidics was used to get monodisperse droplets of the desired size.

The flow velocities of the continuous flow, a DEP saturated 10 mM SDS solution, were varied using a neMESYS Low Pressure Syringe Pump, whereas the dispersed flow (DEP) was set to 100 $\mu\text{L}/\text{h}$. After relaxation of the flow in the device droplets were collected. Different microfluidic devices were used that provided us with various ranges of droplet sizes, depending on the range of interest during the experiments.

3.3.3 Experiments

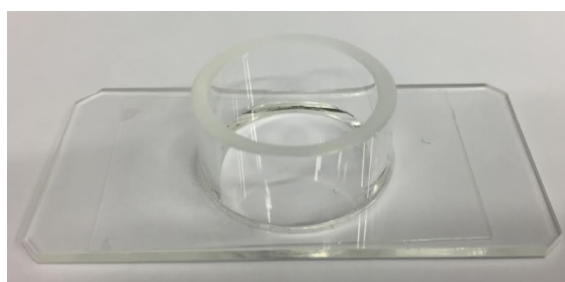


Figure 3.6: The videos were recorded when the DEP droplets were swimming in this sample well.

A sample well was filled with 1 mL 10 mM SDS solution containing PS tracers, and the microscope was focused slightly above the bottom of the well. The microfluidics device was set to produce droplets of the desired size, and after relaxation of the flow through the device a small droplet of the DEP saturated 10 mM solution was dropped into the well.

After droplet addition and the flow relaxed the camera (Phantom Miro eX4-4096mm) on the inverted microscope (Leica DM IL LED) using a 20x objective was set to record at a frame rate of 100 frames per second. We waited until droplets swam into our field of view, and sometimes the focus had to be slightly adjusted. After a typical recording of a few minutes all useful parts of the recording were saved and the sample well was rinsed, 3 times with ethanol to remove traces of oil and 3 times with water. Calculation of the particle sizes was then straight forward when taken the microscope calibration to be 0.9112 pixel/micrometer.

3.3.4 Characterisation

PIV

Particle tracking was used to find the location and radius of the droplet in all frames, this data was used to create a circular mask (from which the size is determined by the obtained radius) at every position. The image stack was loaded into PIVlab and the mask places on top of the droplet to exclude droplet motion in the calculation of the surrounding flow field.

The meshes were set up as follows: the largest one taken had an interrogation area of 128 by 128 pixels which was divided into 64 parts, the second mesh was sized 64 by 64 pixels and accounted for 32 steps. The smallest square had an area of 32 by 32 pixels and partitioned into 16 smaller sections. The rest of the parameters were kept at their default values, and the calculation was run.

After finishing the vector values had to be validated, as it can occur that new tracer particles appear or are related to meshes that are unrealistically far away. Validation is done by manually selecting velocity limits based on a square region in which the majority of the velocity vectors lay and therefore can be considered to be a reliable region. After post-processing the individual PIVlab files were saved and ready for further treatment.

Averaging

The result after applying particle image velocimetry (PIV) is that individual frames are very noisy. This and the enormous extent of frames makes frame-by-frame analysis not doable. Averaging is the solution as it cancels out the random noise, but averaging of a flow field demands some preliminary tasks.

From particle tracking we have obtained a list of coordinates stating the position of the droplet within each frame, the tangent of the difference in y-position divided by the difference in x-position gives a rotation angle with respect to the x-axis α between two sequential frames. In order to average vector fields the droplet centre has to be the middle point of the field, so these positions need to overlap.

Therefore the first step is translating the flow field from the particle position to the origin. The flow around a droplet depends on its orientation, meaning that the second step is rotating the flow field by the obtained rotation angle parallel to the x-axis. As a result all frame-extracted flow fields now have the same centre and orientation and can be averaged.

Upon translating and rotating the average flow matrix becomes larger than initially is recorded, since our recorded flow matrices are rectangular and the droplet position changes. The result is that the velocity vectors at the edges of the profile are averaged over a less amount of frames.

3.4 Results and discussion

3.4.1 Microfluidic size control

Several microfluidic devices have been used to probe the full micrometer size range available with our devices. The smallest available capillaries in our lab have an inner diameter of 0.05 mm, that even become smaller upon tapering. Commercially there are smaller capillaries at hand, but since hand-made manufacturing using the 50 micron tubes was extremely challenging, purchasing the even tinier ones has not been considered. Figure 3.7 shows the experimental data of the largest constructed device. The droplet size depends on the fluid flow velocity set at the syringe pump, where the error bars in 3.7b account for polydispersities in the obtained droplet sizes.

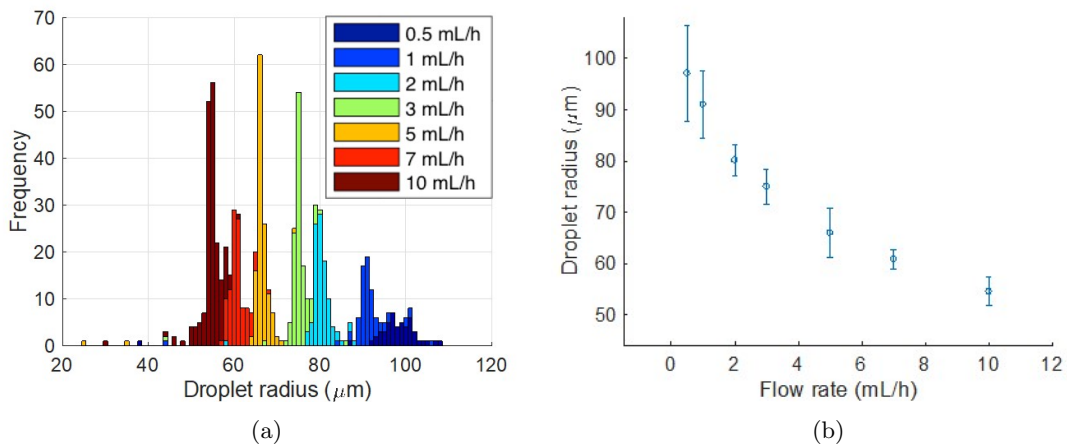
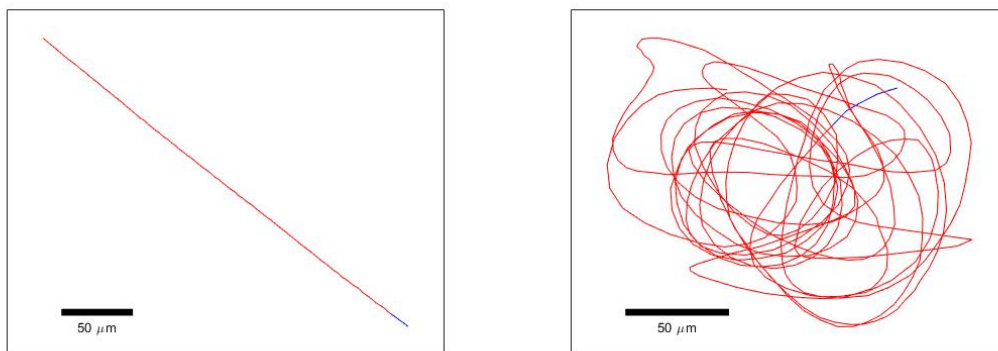


Figure 3.7: Microfluidics statistics in which the dispersed phase is kept constant (at $100 \mu\text{L}/\text{h}$) and the continuous phase is varied to obtain a variety of droplet sizes. The histogram indicate the range of droplet sizes that can be produced using a "large" microfluidic device. The error bars in figure 3.7b represent the polydispersities in the sample.

3.4.2 Swimming dynamics of various sized droplets



(a) Trajectory for a small droplet ($< 35 \mu\text{m}$). (b) Typical trajectory of a large droplet ($\geq 120 \mu\text{m}$).

Figure 3.8: Two experimentally obtained particle trajectories that show typical behavior for the two different swimming regimes.

The trajectories obtained from particle tracking provide us with information about the type of motion performed by the droplets. In figure 3.8 we see two typical trajectories; for a small droplet of $< 35\mu\text{m}$ in size the droplet swims in a straight line, whereas for the large droplet (sized $> 120\mu\text{m}$) we observe not well-defined behaviour that tends to be explained as somewhat random circular motion.

Initially the data was sorted in three regimes; smaller than 35 micron, between 35 and 120 micron and larger than 120 micron, where their movement was linear, curved and undetermined respectively. Since the behaviour of the first two regimes is essentially the same, we compare the swimming behavior of droplets below 35 and above 120 micron. First the mean square displacements of the trajectories from figure 3.8 are analysed, followed by their velocity correlation functions and their changes in swimming direction.

3.4.3 Quantifying the motion of various sized droplets

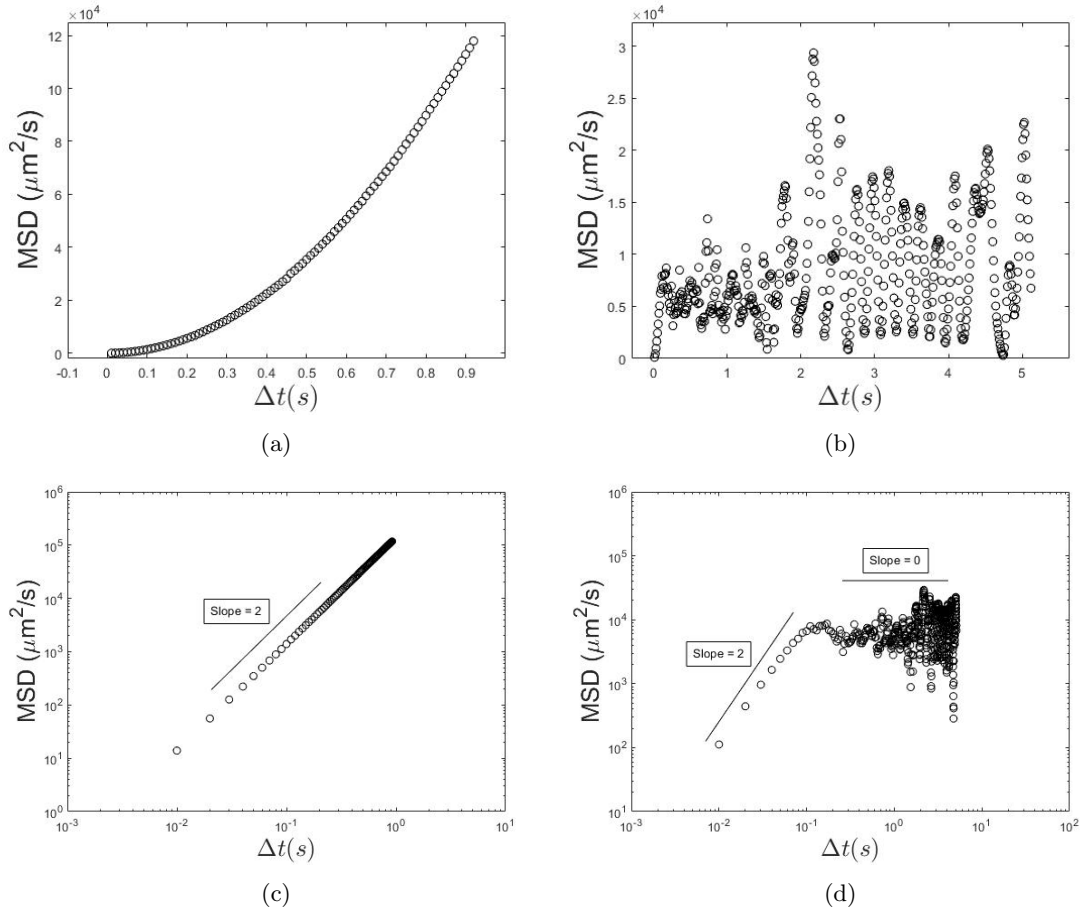


Figure 3.9: Mean square displacements and below their loglog-representations of the trajectories from figure 3.8. Two fundamentally different types of motion are observed, namely: ballistic (a&c) and confined (b&d) motion.

For the small autophoretic droplets ($< 35\mu\text{m}$) we obtain a mean square displacement that is increasing quadratically (figure 3.9a). On the logarithmic scale (figure 3.9c) we see a clear slope of two: a straight trajectory is performing ballistic motion. Droplets that have curved trajectories but swim in a certain direction also exhibit ballistic motion as is determined by MSD analysis. From figure 3.9 b&d we see that for the large droplets only the log-log representation is useful in

unravelling their types of motion. In this plot we see that initially their motion is ballistic and that it quite immediately falls into the confined regime where it remains until all fuel is consumed or when the droplet shrinks below the critical size (of $120\mu\text{m}$).

The question remains why large droplets are confined, but one can speculate about several things: it might be that the force dipole refreshes the fuel supply so fast that the active droplet is constantly situated in optimal conditions. In ideal conditions there will be no tendency to swim to other regions. It might (although it seems less likely) also be the case that the force dipole is biased to one side, inducing such strong rotation that it effectively keeps spinning at its position like a children's spinning top.

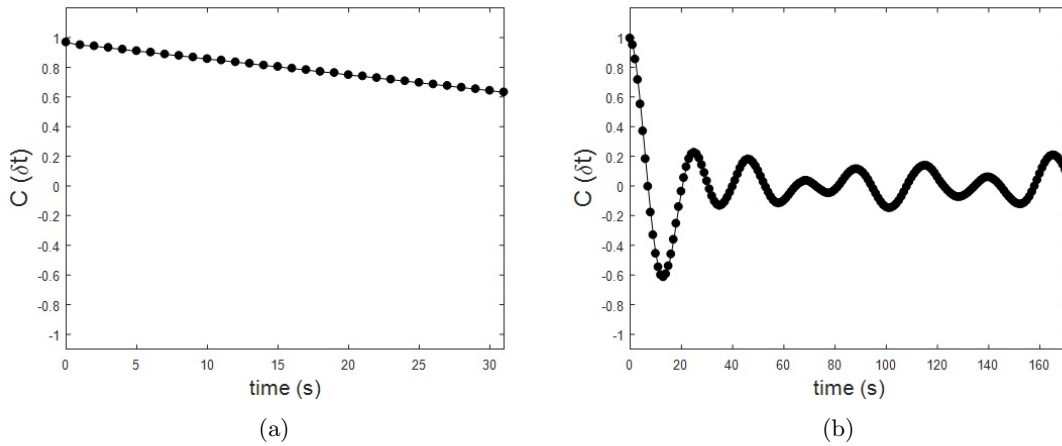


Figure 3.10: Velocity correlation functions of a ballistic (left) and a confined (right) trajectory, calculated based on the trajectories from figure 3.8.

The results obtained from the MSD analysis are confirmed by our findings for the velocity correlation function, and the plot of these calculations can be found in figure 3.10, here again the trajectories from figure 3.8 are used and show the same type of behaviour.

From the decay of the curve information about the rotational diffusion can be extracted, in figure 3.10a we see the ballistically moving droplet that keeps track of its initial direction and therefore slowly (on a time scale of minutes) decays to zero. In figure 3.10b the VCF of the confined droplet's trajectory is shown, that rapidly (on a time scale of seconds) decays beyond zero and keeps oscillating around zero. The fact that the curve continues to oscillate around zero means that the droplet is oscillating and in some way keeps track of its orientation. The oscillation around zero indicates that this is a confined species, whereas diffusive Brownian particles rapidly decay to zero.

When we calculate the persistence time based on random rotation diffusion of 175 microns sized droplet, dispersed in water at 25°C . Those are the conditions of the droplet in 3.10b.

$$\tau_r = \frac{8\pi\eta_f a^3}{k_B T} = \frac{8\pi \cdot (8.9 \cdot 10^{-4} \text{ Pa} \cdot \text{s}) \cdot (87.5 \cdot 10^{-6} \text{ m})^3}{(1.38 \cdot 10^{-23} \text{ J} \cdot \text{K}^{-1}) \cdot 298 \text{ K}} = 3.6 \cdot 10^6 \text{ s}$$

We find that the time it takes to lose memory of its initial direction is about 40 days, thus completely different from what is found by VCF analysis. Calculation for a 30 micron droplet in the same conditions, would obtain a persistence length on the order of hours. This means that in case of isotropic droplets the relation between the persistence time and rotational diffusion does not hold.

Another method to extract information about the persistence of the initial swimming direction is by means of rotation angle analysis, this provides us with knowledge about the frequency a droplet moves either left or right. The trajectories in figure 3.8 are analysed and the obtained angles of rotation are listed in the histograms that is displayed in figure 3.11.

From the trajectories one would expect that small droplets ($\leq 35\mu\text{m}$) that move in straight lines have an average rotation angle close to zero, whereas large droplets ($\geq 120\mu\text{m}$) that have a much more random path have a non-zero average rotation angle. In the figure the rotation angle histograms of those trajectories are shown, where we see that for the small droplet the average indeed lies around zero, whereas the the peak for the large droplet lies off-centred, here shifted to the right. Note that the rotation angles are much more distributed in the right image compared to the left one as can be see by the difference in scaling on the x-axis.

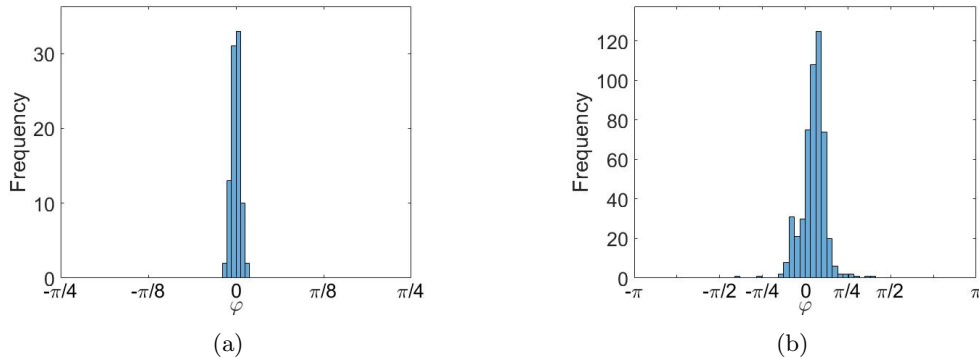


Figure 3.11: Rotation angle histograms of the trajectories from figure 3.8.

The rotation angles histograms produced appear to be normally distributed around the average rotation angle, for a Gaussian distribution this means that the mode, mean and median are identical. The mean angle tells something about the direction of the travelled path as the values of those angles represent the turning direction of the autophoretic droplet. Answers to the question why differently sized droplets demonstrate different behaviour are expected to lie in the surrounding fluid flow fields.

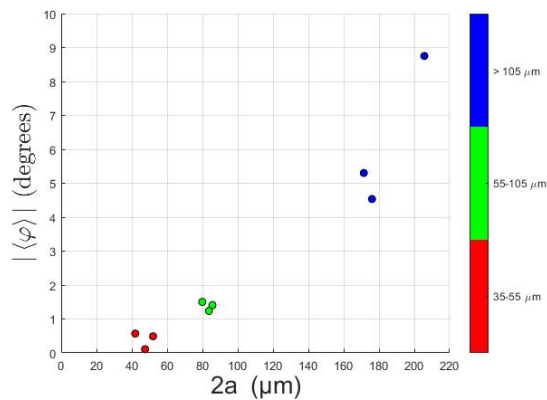


Figure 3.12: The absolute average rotation angle plotted versus the droplet size.

In figure 3.12 we see the absolute average rotation angle with respect to the initial swimming direction plotted against the droplet size. The droplet sizes are averaged over all droplet size values outputted by particle tracking, and since dilution leads to droplet shrinking the size will effectively decrease throughout the recording. Note that we are working with relatively large droplets and that therefore the droplets do not shrink very fast.

From the figure we see the clear trend that the average rotation angle increases upon increasing droplet size. Since we observe linear pathways for $< 35\mu\text{m}$ sized, curved trajectories for $35\text{-}120\mu\text{m}$ and confined tracks for $> 120\mu\text{m}$ sized droplets this seems plausible. Here we need to mention

that the average rotation angle depends on the recording still, as small particles that experience the flow of a neighbouring droplet or a sticking dust particle might be affected by it and therefore perform a curved path.

3.4.4 Visualised flow around various sized droplets

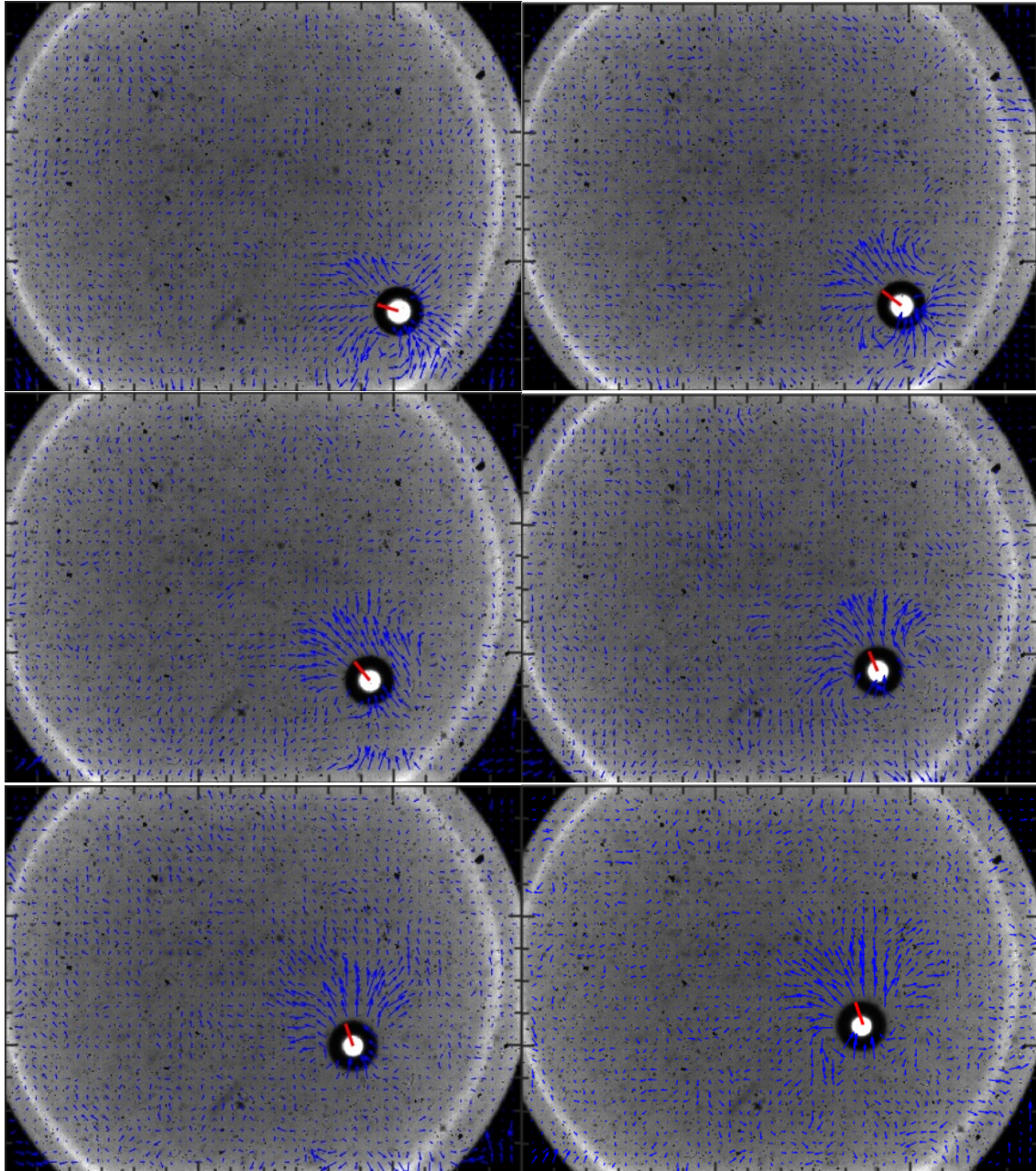


Figure 3.13: Time series for a ballistically moving droplet of about 85 micron in size, surrounded by a source dipole flow field that is averaged in 3.19d. The blue arrows represent the fluid flow whereas the red vector is the velocity of the droplet. Should be proceeded from left to right and from top to bottom.

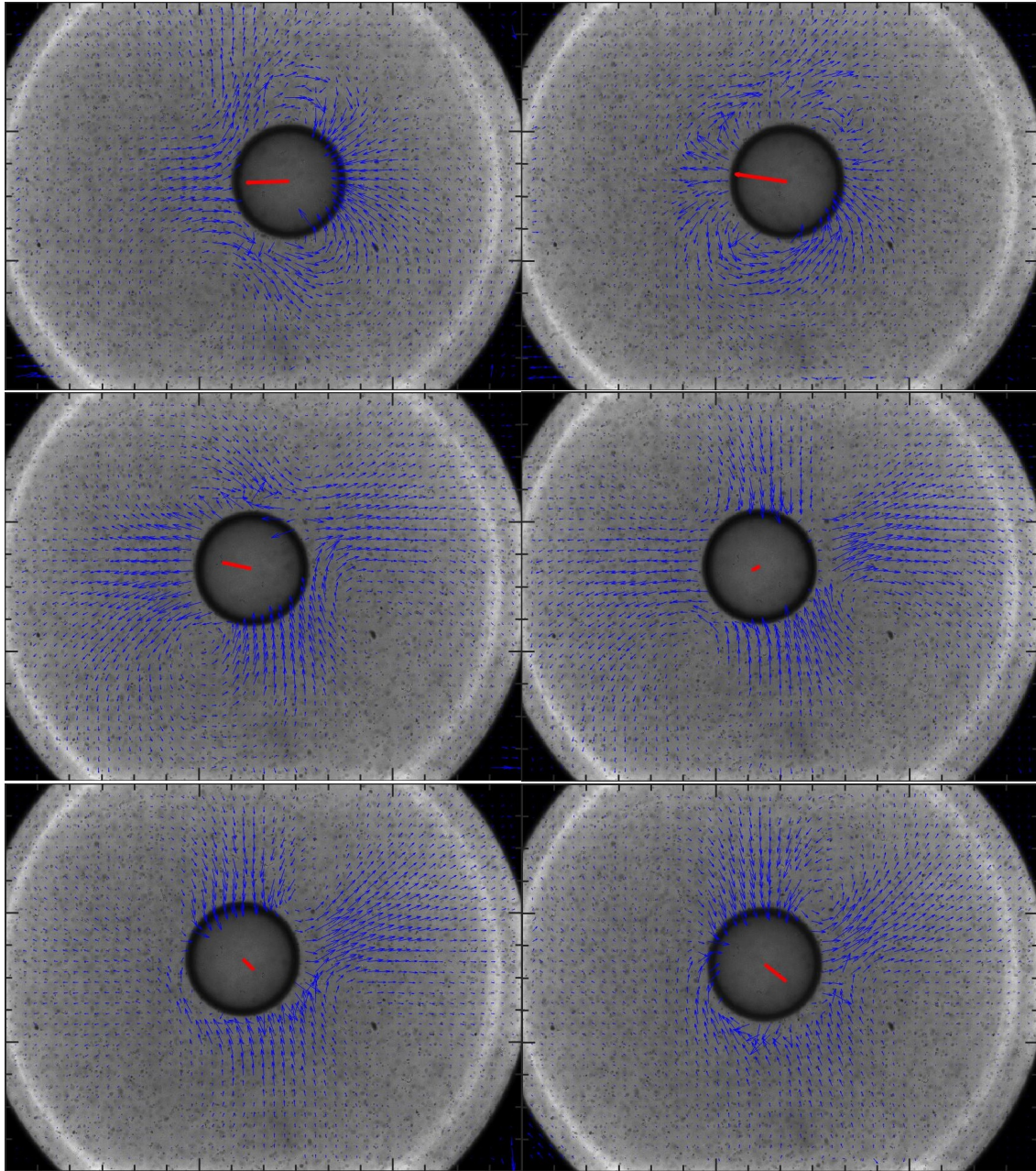


Figure 3.14: Time series of a confined droplet of about 200 micrometer in size. From the flow profile surrounding the droplet in these images the expected average would not merely be a source dipole, as force dipole flow is clearly visible. The calculated average can be found in figure 3.19e. The images should be proceeded from left to right and from top to bottom.

Flow patterns around the swimming droplets were obtained with PIV and two time-series are shown in figures 3.13 and 3.14. From these series we see that both regimes have different types of flow profiles around them. The ballistic time-series presented in figure 3.13 has a source dipole flow field surrounding it. A source dipole is expected as the droplet swims in a straight trajectory without the interference of an external force.

The time-series of the confined droplet shows different behaviour of the flow. In the cases of a large droplet velocity (represented by the red arrow), source dipole flows are seen. However, if the droplet makes a sharp turn and the droplet velocities are low, force dipole flows can be seen.

3.4.5 Average flow profiles of various sized droplets

Frame to frame we see a source dipole for small droplets, as well as a force dipole for big droplets. In order to remove the noise from the images averages were calculated as described in subsection 3.3.4. After averaging, both small and large droplets show a similar flow profile, that looks like a source dipole and are shown in figure 3.15.

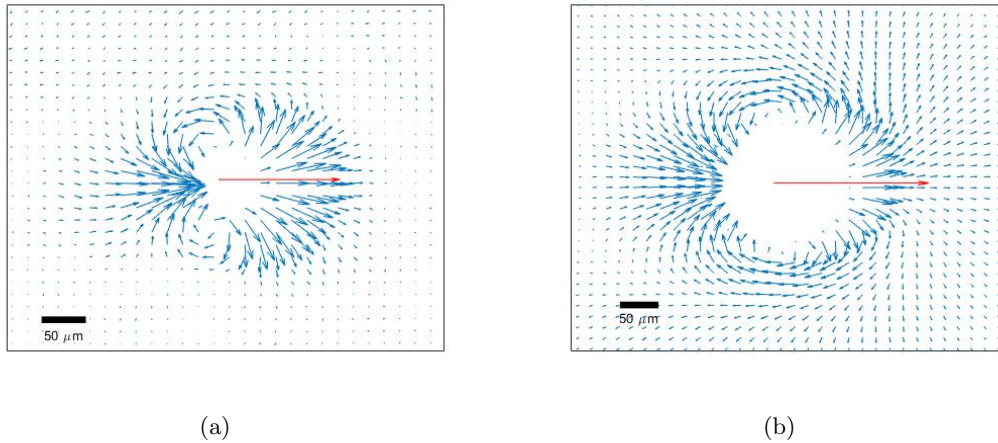


Figure 3.15: Calculated averages of a ballistically moving and a confined droplet. The blue fluid flow vectors are 2 times magnified whereas the red vector indicating the droplet velocity is rescaled to 0.2 times the actual size to fit the image.

The average shown in figure 3.15a is from the ballistically moving droplet that pushes away the fluid on its way, the resulting source dipole flow profile is as expected. For the confined droplet the average in 3.15b does not show the observed force dipole. The thought this observation raised is that the force dipole flow field does not correlate with the swimming direction of the droplet. However, since the swimming direction of these confined droplets appears to be uncorrelated to their initial direction, we are able to correct for biases induced by flow from the third dimension.

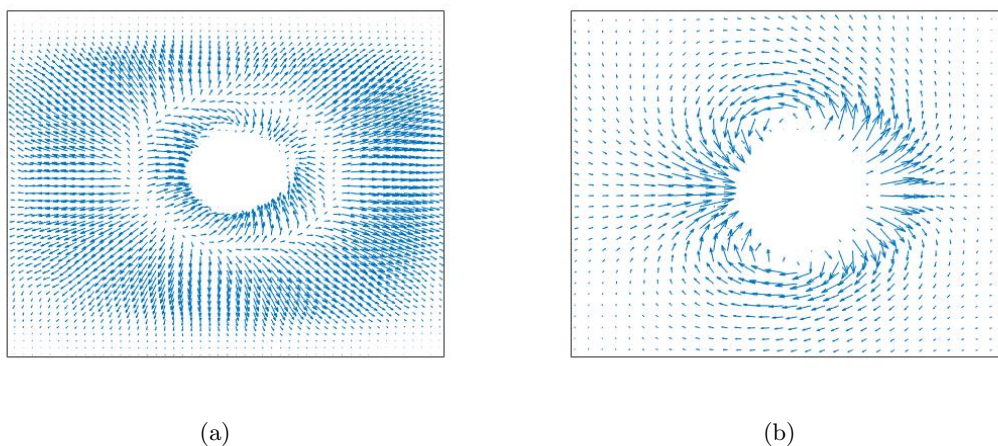


Figure 3.16: In 3.16a we see the non-rotated average that shows no correlation of the fluid velocity and therefore appears as a monopole. When the uncorrelated average is subtracted from the rotated average 3.15b we are still left with a source dipole as can be seen in 3.16b. The averages different approaches from the same droplet as in 3.15b even though the non-rotated looks smaller, this is due to the zoom of the image.

The surfactant flow is downwards in the gravitational direction, since it hardly originates from the glass walls. This means that the third dimensional flow (near the droplet's surface) will slip the droplet's surface and spread out isotropically. Therefore the result upon averaging flow profiles, is that some biases are present as third dimensional flow is present. To account for this a new average (for the confined droplets) was calculated by translating the flow profiles to the origin but omitting the rotation (3.16a), which results in a monopolar flow profile in which all the fluid flow vectors are uncorrelated.

Subtracting the uncorrelated average from the rotated average was done in order to account for the third dimension. The non-rotated as well as the subtracted average related to this approach can be found in figure 3.16.

3.4.6 Radial decay of the (tangential) velocity

In order to quantify our obtained average flow fields decays of the fluid flow velocity were calculated. Radial decays were calculated to obtain information about the magnitude of the flow velocities, and tangential (perpendicular to the swimming direction) decay calculations were done to quantify our findings and relate our profiles to predictions done in the literature.

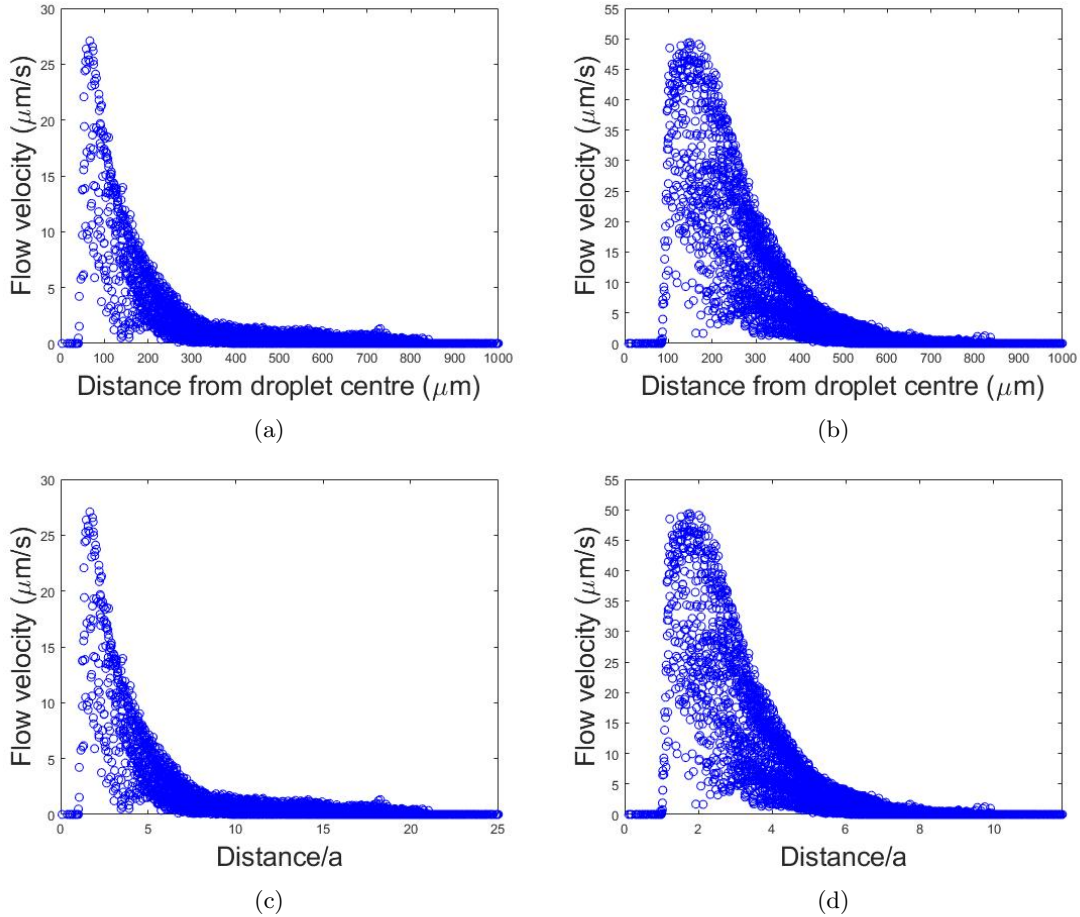


Figure 3.17: Radial decays of the flow velocities of droplets of ~ 80 and $\sim 200 \mu\text{m}$ in size, and the same decays scaled to the droplet radius a .

When comparing the images of figure 3.17a & 3.17b we see that the fluid velocity of the larger droplet reaches higher velocity values than the smaller one, which shows that the magnitude of the flow is higher around larger droplets. Note that the the fluid velocity is zero at the start of the

decay, at distances shorter than the droplet radius, meaning that the droplet size can be extracted from the unscaled decays.

If we divide the distance from the droplet centre by the droplet radius (figure 3.17c & 3.17d), we see that the radial decay is actually proportional to the size of the droplet, and that the surrounding flow field that is induced by a droplet is typically on the order of 3-4 times the diameter of the droplet. Six times the droplet radius is taken as the value for the cut-off parameter in the symmetry analysis. This radius is used to set a boundary outside which the remaining flow is assumed not to be related to the droplet movement.

Setting this measure for fluid flow symmetry to the lowest radius value is due to a practical restriction. Our fluid flow profiles are averaged over a certain amount of frames in which these droplets are 3 times the radial distance away from the edge of the frame. By doing this we assure the calculated average to have an equal amount of fluid vectors on each over the averaged fluid positions, whereas when we make the cut-off radius too large, the remaining frames would simply not suffice for a reliable average.

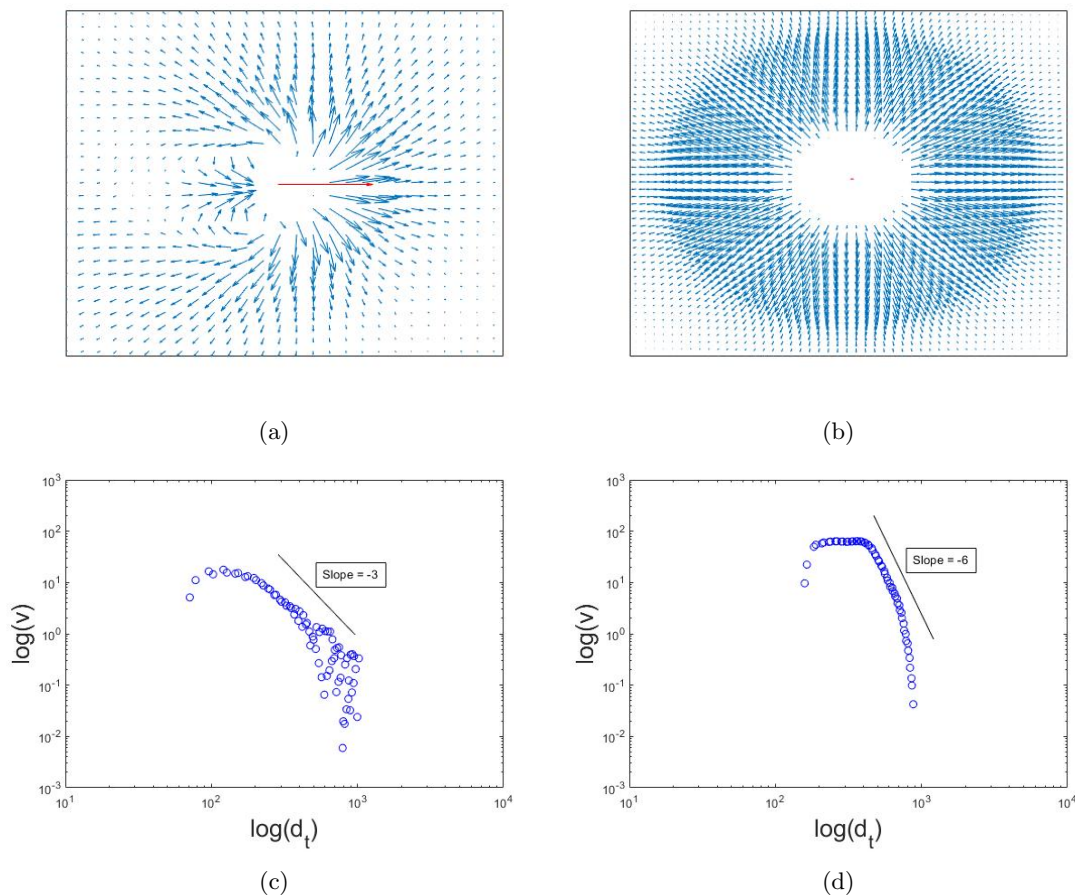


Figure 3.18: In 3.18c we see the log of the tangential decay of a source dipole flow field, obtained from the same droplet as the average in figure 3.18a and the radial decay from 3.17a. Subfigures b&d show the average flow field of a monopole and its tangential decay respectively.

Radial decays in the tangential direction are taken for the source dipole and the monopole. In the case of the monopole the direction of decay is not important since the fluid propagates evenly in each direction, but for convenience the tangential direction is taken to be the y-axis assuming that the centre of mass lies at the origin, which is the case as upon averaging all fluid flow field are translated to the origin.

From the tangential decay in figure 3.18c we conclude that the decay of the source dipole indeed decays with a^{-3} , as was predicted by Spagnolie et al. According to figure 3.18d the monopole decays proportional to a^{-6} meaning that the monopolar contribution to the flow is eclipsed by the effect of the source dipole pusher.

3.4.7 Relating the droplet motion to the fluid flow

The symmetry analysis is introduced trying to connect the trajectories to their surrounding flow fields. The symmetry number σ_S contains information about the degree of symmetry in an average flow profile and will be coupled to the average rotation angle that we obtained from our trajectories. We have seen for larger droplets that the mode angle lies off-centered and from our velocity decays we concluded that the fluid flow around a droplet is mostly decreased at a radial distance three times the droplet diameter ($6a$).

What we see from figure 3.20 is that there is a correlation between the obtained average flow profiles and the direction changes the droplets make in their trajectories. It seems that the larger the droplet the bigger the symmetry number. This trend is biased because different amounts of data points have been processed, as the cut-off radius is based on the droplet size, whereas the vector spacing remains the same.

The cut-off radius increases (area of $\pi(3a)^2$) with the increase in droplet size (area of πa^2), whereas the spacing between velocity vectors remains the same, meaning that upon increasing cut-off radius more velocity vectors are considered leading to more related vectors that possibly deviate from the perfect symmetry and therefore an increase in the overall symmetry number.

To overcome biased amount of vectors it could be tried to use different microscope magnifications or adjust the PIV mesh size, but this demands different tracer concentrations as well.

In figure 3.19 some trajectories and their corresponding averages are shown, table 3.1 states all average rotation angles and the symmetry numbers that are plotted in figure 3.20, also figure 3.12 is based on the values stated in this table. The obtained symmetry numbers are based on a selection of visually reasonable averages, but flow from the third dimension plays a vital role.

Table 3.1: Numerical data of the average rotation angles and symmetry numbers that are plotted in figure 3.20, here also the droplet sizes are stated and the ones indicated with an asterisk are shown in figure 3.19.

Particle size ($2a$)	Average rotation angle ($\langle\langle\varphi\rangle\rangle$)	Symmetry number (σ_S)
$\sim 42\mu\text{m}$	-0.5705 degrees	1.1762
$\sim 48\mu\text{m}^*$	-0.1087 degrees	0.0649
$\sim 52\mu\text{m}$	0.4890 degrees	-1.2355
$\sim 80\mu\text{m}$	-1.5020 degrees	1.7757
$\sim 84\mu\text{m}^*$	-1.2365 degrees	4.5332
$\sim 86\mu\text{m}$	1.4081 degrees	4.3950
$\sim 171\mu\text{m}$	-5.3041 degrees	-82.6949
$\sim 176\mu\text{m}^*$	-4.5357 degrees	-39.4738
$\sim 205\mu\text{m}^*$	8.7530 degrees	-10.6217

If a droplet is fully in focus, the plane of view is not exactly positioned at the centre of the droplet. Assuming a surfactant supply from upstream, a focus plane below the symmetry plane through the centre of mass would isotropically point outward from the droplet centre. The observed fluid flow below the desired plane of view is that of a monopole (figure 3.18b). Taken this into account, movement of the droplet in the third dimension biases the calculated average.

As mentioned earlier, we can correct for the third dimension in the case of large confined droplets. The symmetry numbers calculated for those droplets are based on the subtracted average in which we attempted to cancel out the third dimensional flow.

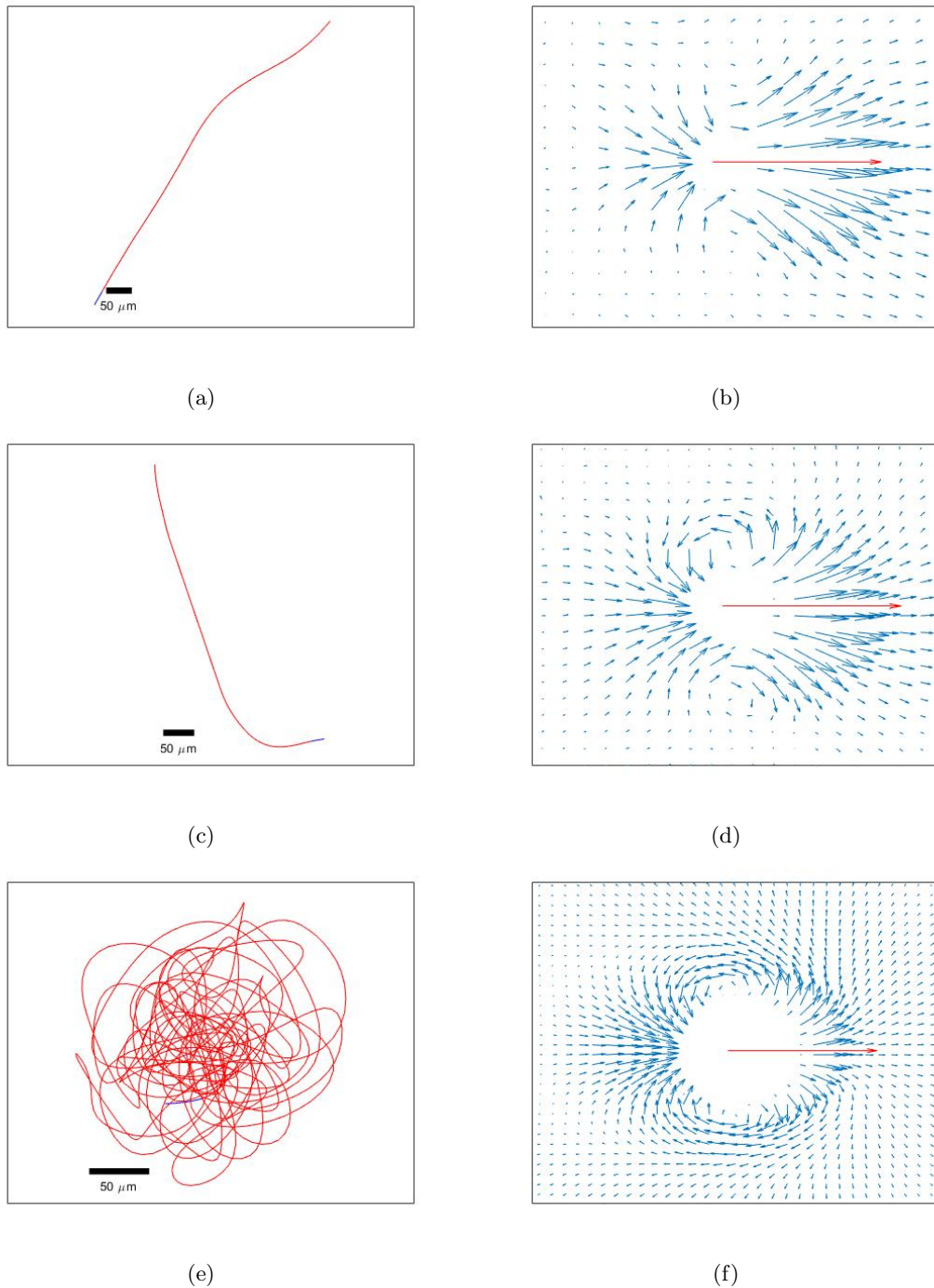


Figure 3.19: Subfigure a&b belong to a $\sim 50 \mu\text{m}$, c&d to a $\sim 85 \mu\text{m}$ and e&f to a $\sim 175 \mu\text{m}$ droplet. A typical path for the smallest sized droplet is not shown here as the averages observed for those are too noisy to be fit for symmetry analysis. Here are all blue fluid flow arrows the same size (2 times magnified) whereas the red droplet velocity arrows are rescaled by a factor 0.2 to fit the image for clarity.

To show the complexity of fluid dynamics as a three dimensional phenomena a experimentally obtained image is show in figure 3.21, in which the assumption of surfactant supply from the

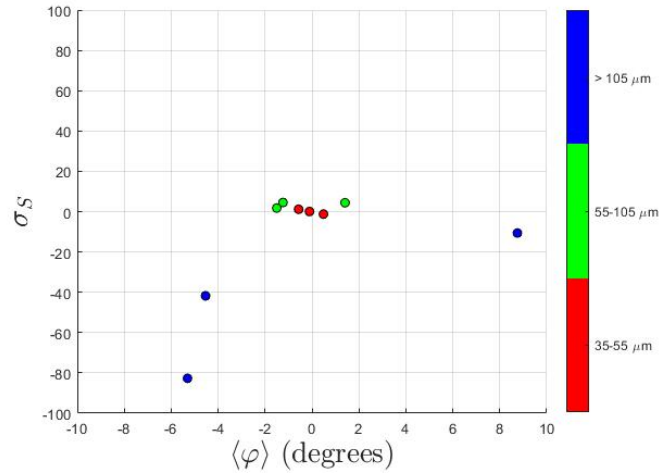


Figure 3.20: The symmetry numbers plotted versus the average rotation angle of droplets that have different types of trajectories as function of their droplet size. The red points are droplets ranging from 35-55 μm , the green ones are between 55-105 μm and the blue dots are droplets larger than 105 μm .

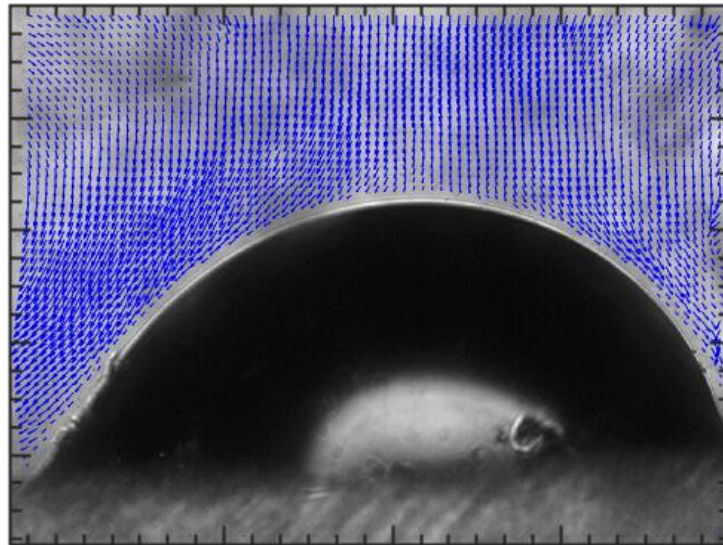


Figure 3.21: Experimentally obtained side view average of fluid flow, taken using a tilted microscope to observe the xz -plane of a tremendously large droplet of approximately 1 mm in size.

liquid-air interface is confirmed. Theoretically confocal microscopy could serve as an option to study active particles in the third dimension, but this is practically undoable as active particles move too fast for the confocal to capture the surrounding movement, meaning that the confocal speed is the limiting factor.

3.5 Conclusions

In the case of isotropic droplets there exist a critical size ($\sim 120 \mu\text{m}$ at 10 mM SDS) below which ballistic motion is observed, when the droplet size exceeds this critical size, MSD and VCF analysis show these autophoretic droplets to be confined in space.

Averaging by translation and rotation based on the droplet its swimming direction results in a source dipole flow field that thus is correlated to the swimming direction. The force dipole flow field that is observed around confined droplets does not correlate with the swimming direction and therefore a new way of averaging should be proposed in order to experimentally observe force dipole fields.

The magnitude of the fluid flow velocity is larger around larger droplets than around smaller ones, but upon quantification of the source dipole flow field we observe a a^{-3} decay in the tangential flow velocity, a decay which is in agreement with the literature. For the isotropic monopole a tangential velocity decay of a^{-6} is found, a decay that as far as we are aware has not been mentioned before in the literature.

When reliable data is handled the absolute average rotation angle increases with droplet size. Tiny droplets ($< 35 \mu\text{m}$) propel in a straight line whereas big droplets ($> 120 \mu\text{m}$) perform some sort of random circular path as they are confined.

Microfluidics proved to be a useful tool to probe the different size ranges of these droplets and varying capillary sizes in different devices allows us to obtain a wide range of droplet sizes, ranging from $10 \mu\text{m}$ to over $200 \mu\text{m}$ in diameter.

The symmetry number approach did not turn out to be very useful. However the possibility still exists that there is a correlation between the flow profile and the droplet trajectories. Because our symmetry approach did not provide us with enough statistics another way has to be found to relate the fluid flow profile to the observed droplet trajectories.

Chapter 4

Conclusions

Recorded experiments on isotropic droplets and their surrounding fluid have gained insight in the motion and dynamics of these droplets. As for many phoretic particle transports their self-propulsion is driven by chemical gradients that direct the motion. It has been shown that for dissolution below the critical Péclet number the Marangoni flow can be written as a slip-velocity which is capable to enhance the sedimentation velocities of falling droplets. Therefore we were able to qualitatively prove that the equation derived by Moerman et al. [22] holds in the diffusion limited case below the critical Péclet number.

Above the critical Péclet number ($Pe = 4$) self-propulsion occurs which leads to different types of motion depending on the droplet size. The critical size lies around $120 \mu\text{m}$, below which the droplet moves ballistically induced by the surrounding source dipole flow field. When the droplet exceeds the critical size its flow is dominated by a force dipole, even though this flow field does not contribute to the propulsion it for an unknown reason results in the confinement of the droplet at a certain position in the medium.

From the averaged source dipole and monopole the tangential decay curves were obtained and their logarithmic linearisations showed flow perturbations that decay as $\sim 1/r^3$ and $\sim 1/r^6$ respectively. In the case of the source dipole this confirms the theoretical prediction for this specific flow field. The monopole decay of $\sim 1/r^6$ has, as far as I know, not been reported earlier. Since this decay is observed below the plane of interest, it seems plausible that it has not been reported before.

Analysis based on the symmetry number does not appear to be very reliable since extremely neat data is required. It also contains biases as the cut-off radius that is related to the mesh size. But even though a clear correlation between the average rotation angle and the symmetry number was not found. Future techniques are hoped to provide us with relations between the droplet trajectories and their neighbouring flow fields.

Bibliography

- [1] Emergence: A unifying theme for 21st century science. <https://medium.com/sfi-30-foundations-frontiers/emergence-a-unifying-theme-for-21st-century-science-4324ac0f951e>. Accessed: 2018-12-20. 1
- [2] Nuclear Power, Friction Factor for Laminar Flow. <https://www.nuclear-power.net/nuclear-engineering/fluid-dynamics/major-head-loss-friction-loss/friction-factor-for-laminar-flow/>. Accessed: 2018-12-03. 57
- [3] J. Anderson. Colloid Transport By Interfacial Forces. *Annual Review of Fluid Mechanics*, 21(1):61–99, 1989. 7, 8, 24, 25
- [4] Daniel L. Blair and Eric R. Dufresne. Matlab particle tracking code. <http://site.physics.georgetown.edu/matlab/>, 2008. 11
- [5] Aidan Brown and Wilson Poon. Ionic effects in self-propelled Pt-coated Janus swimmers. *Soft Matter*, 10(22):4016–4027, 2014. 3
- [6] F. Bueche and M. Davison. Viscosity-temperature relation for diethyl phthalate [9]. *The Journal of Chemical Physics*, 45(11):4361–4362, 1966. 9
- [7] John C Crocker and David G Grier. Methods of Digital Video Microscopy for Colloidal Studies. *Journal of Colloid and Interface Science*, 179(179):298–310, 1996. 11
- [8] Knut Drescher, Jörn Dunkel, Luis H. Cisneros, Sujoy Ganguly, and Raymond E. Goldstein. Fluid dynamics and noise in bacterial cell – cell and cell – surface scattering. *Proceedings of the National Academy of Sciences*, 108(27):10940–10945, 2011. 24
- [9] Albert Einstein. Über die von der molekularkinetischen Theorie der Wärme geforderte Bewegung von in ruhenden Flüssigkeiten suspendierten Teilchen. *Annalen der Physik*, 322(8):549–560, 1905. 21
- [10] J. Elgeti, R. G. Winkler, and G. Gompper. Physics of microswimmers - Single particle motion and collective behavior: A review. *Reports on Progress in Physics*, 78(5), 2015. 1
- [11] Ramin Golestanian, Tanniemola B. Liverpool, and Armand Ajdari. Propulsion of a molecular machine by asymmetric distribution of reaction products. *Physical Review Letters*, 94(22):1–4, 2005. 2
- [12] Paul V.C. Hough. Method and means for recognizing complex patterns. *U.S. Patent 3,069,654*, Dec. 18, 1962. 11
- [13] Jonathan R. Howse, Richard A L Jones, Anthony J. Ryan, Tim Gough, Reza Vafabakhsh, and Ramin Golestanian. Self-Motile Colloidal Particles: From Directed Propulsion to Random Walk. *Physical Review Letters*, 99(4), 2007. 1, 2, 21
- [14] Douglas L Inman. Sorting of sediments in the light of fluid mechanics. *Journal of Sedimentary Research*, 19(2):51–70, 1949. 9

- [15] Rustem F. Ismagilov, Alexander Schwartz, Ned Bowden, and George M. Whitesides. Autonomous movement and self-assembly. *Angewandte Chemie - International Edition*, 41(4):652–654, 2002. 2
- [16] Ziane Izri, Marjolein N. Van Der Linden, Sébastien Michelin, and Olivier Dauchot. Self-propulsion of pure water droplets by spontaneous marangoni-stress-driven motion. *Physical Review Letters*, 113(24), 2014. 2, 5, 9
- [17] Chenyu Jin, Carsten Krüger, and Corinna C. Maass. Chemotaxis and auto-chemotaxis of self-propelling artificial droplet swimmers. *Proceedings of the National Academy of Sciences of the United States of America*, 114(20):5089–5094, 2016. 2
- [18] F. Jülicher and J. Prost. Generic theory of colloidal transport. *European Physical Journal E*, 29(1):27–36, 2009. 7, 25
- [19] W. Lee, H. Amini, H. A. Stone, and D. Di Carlo. Dynamic self-assembly and control of microfluidic particle crystals. *Proceedings of the National Academy of Sciences*, 107(52):22413–22418, 2010. 2
- [20] Sébastien Michelin and Eric Lauga. Phoretic self-propulsion at finite Péclet numbers. *Journal of Fluid Mechanics*, 747:572–604, 2014. 7
- [21] Sébastien Michelin, Eric Lauga, and Denis Bartolo. Spontaneous autophoretic motion of isotropic particles. *Physics of Fluids*, 25(6):1–7, 2013. 5, 6, 7, 8, 9, 20
- [22] Pepijn G. Moerman, Henrike W. Moyses, Ernest B. Van Der Wee, David G. Grier, Alfons Van Blaaderen, Willem K. Kegel, Jan Groenewold, and Jasna Brujic. Solute-mediated interactions between active droplets. *Physical Review E*, 96(3):1–8, 2017. 5, 6, 8, 9, 18, 42
- [23] Pepijn G Moerman, Henrike W Moyses, Ernest B Van Der Wee, David G Grier, Alfons Van Blaaderen, Willem K Kegel, Jan Groenewold, and Jasna Brujic. Solute-mediate Interactions Between Active Droplets Supplementary Information. pages 1–19, 2017. 5
- [24] Pasupati Mukerjee and Karol J. Mysels. Critical Micelle Concentrations of Aqueous Surfactant Systems. *Journal of Pharmaceutical Sciences*, 61(2):319, 1972. 4
- [25] Liselotte Olthof. Mapping of the flow around shrinking DEP droplets. 2016. 23, 26
- [26] Jeremie Palacci, Stefano Sacanna, Asher Preska Steinberg, David J Pine, and Paul M Chaikin. Colloidal Surfers. *Science*, 339(February):936–939, 2013. 2
- [27] Walter F. Paxton, Kevin C. Kistler, Christine C. Olmeda, Ayusman Sen, Sarah K. St. Angelo, Yanyan Cao, Thomas E. Mallouk, Paul E. Lammert, and Vincent H. Crespi. Catalytic nanomotors: Autonomous movement of striped nanorods. *Journal of the American Chemical Society*, 126(41):13424–13431, 2004. 2
- [28] Simon J.K. Pedersen. Circular Hough Transform. *Aalborg University, Vision, Graphics, and*, (November):1–6, 2007. 11
- [29] Albert P. Philipse. *Brownian Motion, Elements of Colloid Dynamics*. Van ’t Hoff Laboratory for Physical and Colloid Chemistry, Utrecht University, Padualaan 8 3584 CH Utrecht, 8 2018. 56
- [30] Marco Polin, Idan Tuval, Knut Drescher, J. P. Gollub, and Raymond E. Goldstein. Chlamydomonas swims with two "gears" in a eukaryotic version of run-and-tumble locomotion. *Science*, 325(5939):487–490, 2009. 1, 24
- [31] E M Purcell. Life at low Reynolds number. *Am.J.Phys.*, 45(1):1–11, 1977. 1

- [32] Yuri S. Ryazantsev, Manuel G. Velarde, Ramón G. Rubio, Eduardo Guzmán, Francisco Ortega, and Pilar López. Thermo- and soluto-capillarity: Passive and active drops. *Advances in Colloid and Interface Science*, 247(April):52–80, 2017. 2
- [33] Saverio E. Spagnolie and Eric Lauga. Hydrodynamics of self-propulsion near a boundary: predictions and accuracy of far-field approximations. *Journal of Fluid Mechanics*, 700:105–147, 2012. 25
- [34] Snigdha Thakur and Raymond Kapral. Collective dynamics of self-propelled sphere-dimer motors. *Physical Review E - Statistical, Nonlinear, and Soft Matter Physics*, 85(2):1–8, 2012. 22
- [35] William Thielicke and Eize J. Stamhuis. PIVlab - Towards User-friendly, Affordable and Accurate Digital Particle Image Velocimetry in MATLAB. *Journal of Open Research Software*, 2(1):e30, 2014. 23
- [36] Shashi Thutupalli, Ralf Seemann, and Stephan Herminghaus. Swarming behavior of simple model squirmers. *New Journal of Physics*, 13(July), 2011. 2
- [37] Taro Toyota, Naoto Maru, Martin M Hanczyc, Takashi Ikegami, and Tadashi Sugawara. Self-Propelled Oil Droplets Consuming "Fuel" Surfactant. *Journal of the American Chemical Society*, 131(14):5012–5013, 2009. 5
- [38] A. van Blaaderen, M. Dijkstra, R. van Roij, A. Imhof, M. Kamp, B. W. Kwaadgras, T. Vissers, and B. Liu. Manipulating the self assembly of colloids in electric fields. *European Physical Journal: Special Topics*, 222(11):2895–2909, 2013. 2
- [39] Wei Wang, Wentao Duan, Suzanne Ahmed, Ayusman Sen, and Thomas E. Mallouk. From one to many: Dynamic assembly and collective behavior of self-propelled colloidal motors. *Accounts of Chemical Research*, 48(7):1938–1946, 2015. 2
- [40] Xiaolu Wang, Martin In, Christophe Blanc, Maurizio Nobili, and Antonio Stocco. Enhanced active motion of Janus colloids at the water surface. *Soft Matter*, 11(37):7376–7384, 2015. 2
- [41] Andreas Zöttl and Holger Stark. Emergent behavior in active colloids. *Journal of Physics Condensed Matter*, 28(25), 2016. 22, 24, 25

Appendix A

Fabrication of microfluidic devices

Accessories

1. A glass slide (Thermo Scientific Menzel-Gläser, 76 x 26 mm cut edges)
2. Three different sized capillaries (VitroCom, VitroTubes™ for example:
0.5 mm square ID, 0.7 mm OD Cat.# 8250
0.2 mm square ID, 0.4 mm OD Cat.# 8320-050
0.1 mm round ID, 0.17 mm OD Cat.# CV1017-B-100)
3. Two different types of needle tips
(Small: Techsil Tip Dispenser 21g Blunt End Tip Green
Large: BD Microlance 21g x 2", 0.8 x 50 mm Green)
4. Tubing (BOLA Tubing, ID: 0.8 mm, OD: 1,6 mm, Wall thickness 0.4 mm)
5. Glue (3M Scotch-Weld™ Epoxy Structural Adhesive DP100)
6. A retort stand
7. A retort bosshead
8. A retort clamp
9. Two paper clamps
10. A gas burner
11. A glass cutting blade (zirconium oxide)
12. Two combination pliers
13. An optical microscope or a magnifying glass

The first step is to prepare the tapered capillary, for that we place a paper clamps (protected by a small piece of paper towel) on both sides of the smallest (round) capillary and hang it with one clamp at the adjusting screw of our retort clamp (that is placed inside the bosshead on our retort stand). By fastly going back and forth with the gas burner, using a blue flame, the glass will locally melt and the weight of the bottom clamp suffices to stretch out the capillary. Remove the capillary delicately from the clamps and place it on a flat surface, cutting it at the thinnest part with a glass cutting blade provides us with two tapered capillaries.

The next step is preparing the foundation of the device. Therefore we place the glass slide at the flat surface and place the largest (square) capillary exactly in the middle and glue it with two tiny drops of glue (approximately 0.5 cm away from edges of the capillary) onto the glass slide.

When the glue has dried, the smallest (tapered) capillary is shoved in from the left side and the intermediate capillary is shoved in from the right. The microscope (or magnifying glass) is used to determine whether the smallest capillary reaches inside the intermediate one, once this succeeded both extending capillaries are glued (about 0.5 cm away from the edge of the outermost square capillary) onto the glass slide.

Two needle tips are taken and two small carvings are made on opposite sides of the plastic (for very tiny capillaries this is not necessary). The carved tips (that serve as inlet and flush) are place upside down between the drops of glue, such that the ends of the outermost capillary are located under the tips, and the tips are carefully glued onto the glass slide making sure that no glue spreads under the tip (and possibly blocks the entrance of the square capillary).

The last step is to solidify the extending capillary edges for workability and strength of the device. We take two more needle tips and clamp them at the metal to plastic transition into the combination plier, and remove the plastic parts by gently bending the plastic back and forth. Once the metal parts are loosened another combination plier is used to bend the metal to a ninety degree angle. The metal needles are carefully placed around the extending parts of the smallest and intermediate capillary and extensively glued onto the glass slide (making sure that the only passage for the liquid is at the ends).

Once the glue has dried, tubing can be connected to the inlets, the dispersed phase is connected to the bend needle connected to the innermost (tapered) capillary and the continuous phase is connected to the carved tip on the opposite side of the device. Upon usage the flush is shut (for example by a small piece of tubing connected to tip that is filled with glue for closing) and tubing for both phases is connected to a syringe pump. Collection of the monodisperse droplets occurs from the metal needle that is located at the side of the continuous flow inlet (a schematic illustration is provided in the main text in figure 2.5).

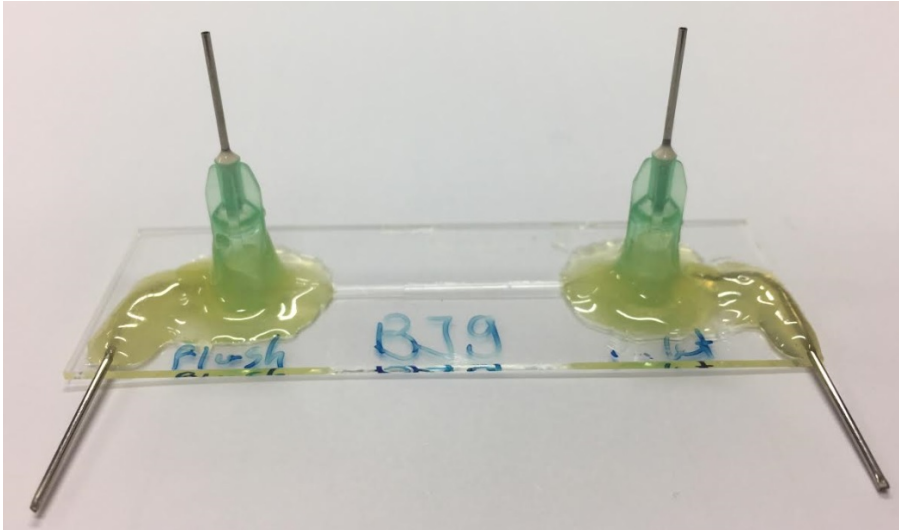


Figure A.1: Microfluidic device hand-crafted via the approach mentioned above, leading to the droplet size range as is shown in Chapter 3. This device is build out of an outer 0.5 mm square ID, a intermediate 0.2 mm square ID and a innermost 0.1 mm round ID capillary.

Appendix B

Particle tracking algorithm

```
%% Particle location and size in time
% Purpose: track a set of particles moving over time in 2 dimensions and
% Expected input: imagestack containing one or more particles of size r.
%     lower and upper boundary of r should be defined below
% Output format: matrix 'tr' of particle position and size in time:
%     [x, y, size, time, particle ID], also output as txt file.
%     image with tracks coloured by particle ID
% Uses code by Blair and Dufresne: http://site.physics.georgetown.edu/matlab/
% Created by Pepijn Moerman at 25-04-2016
% Last modified in June 2018 by Bertjan van Dijk
% Output:    - textfile with
%            - image with tracks coloured by particle ID
% Uses additional codes: track()

%% Parameters
directory = 'E:/Microscopedata/Sedimentation/6mM_SDS/10x_6mMSDS_sed0014/';
name = '10x_6mMSDS_sed0014';

fname = [directory name '.tif'];
% Indicate name under which to save output text file
fsave = [directory name '_trace.txt'];

% Set parameters for circular Hough transform
diameter = 12;
rlower = diameter/2 - 2; % lower bound initial particle size in pixel
rupper = diameter/2 + 2; % upper bound initial particle size in pixel
sensitivity = 0.92;      % sensitivity for particle find: 1 finds every
                        % contrast difference, 0 finds no contrast difference

% Set preferences for printing image, inverting contrast and num_images used.
invert = 1;              % '1' is invert contrast, '0' is not invert contrast
                        % invert if particle is darker than surrounding
num_images = 0;         % '0' is use all images in stack. 'n' (is not 0) uses
                        % first n images from stack it is recommended to start
                        % with num_images=1 to test values below
output = 1;             % '1' is create output, '0' is create no output
trackcheck = 1;        % '1' is perform tracking, '0' is perform no tracking
```

```

PIVcheck = 1;          % '1' if image will be used for PIV later. Creates a
                      % contour to use in PIVlab. '0' if not.
particleskipper = 0; % skip particile finder: yes='1',no='0'
                      % put yes if you want to change output, without finding
                      % particles all over again

% Set parameters for tracking software
maxdisp = 50;        % maximum displacement
param.mem = 0;       % how long particle can go missing
param.dim = 2;       % dimensionality of data
param.good = 10;     % how long track needs be to be accepted
param.quiet = 1;    % 0 = text, 1 = no text

%% Checks on parameters and image
% Assert good value for num_images
info = imfinfo(fname);
if num_images > numel(info)
    error('num_images is larger than stacksize: use a smaller value or ...
          "0" to use entire stack')
end

% Extract numer of images from stack
if num_images == 0
    num_images = numel(info);
end

%% Particle finder
% Skip section to use values from previous run
if particleskipper == 0
    % define matrices
    A = [];
    centers = [];
    radii = [];
    pos = [];
    radiistack = [];
    percentage = 0;

    % For all images in stack
    for k = 1:num_images
        A = imread(fname, k);
        if k/num_images > percentage
            percentage = percentage + 0.05;
            ['Particle tracking process: ' num2str(100*percentage) '%']
        else
            % Do nothing
        end
    end

    % Invert contrast if invert = 1
    if invert == 1
        A = 255 - A;
    end
end

```

```

% Track droplet centers and radii
% centers = [x, y], radii = [r]
%%%%%%%%%% imfindcircles() PERFORMS THE CIRCULAR HOUGH TRANSFORM !!!
[centers, radii] = imfindcircles(A, [round(rlower), round(rupper)], ...
    'sensitivity', sensitivity);

% Add image number to radii
radii(:, 2) = k;
% Add image number to centers
centers(:, 3) = k;
% Append position matrix with new found centers
% and select only the most dominant circle
pos = [pos centers(1, :)];
% Append radii stack matrix with new found radii
% And select only the radius of the most dominant circle
radii_stack = [radii_stack radii(1, :)];
end
end

%% Tracking
tr = [];
% Check if tracking is desired
if trackcheck == 1 && num_images ~= 1
    % Run trackingcode:
    % This code connects the locations of the same particle and numbers them
    %%% track() IS THE COMBINATORIAL ALGORITHM BY BLAIR AND DUFRESNE !!!
    tr = track(pos, maxdisp, param);
end

%% Check for missing frames
missedframes = [];
for i = 1:length(tr(:, 3))
    if i ~= tr(:, 3)
        missedframes(end + 1) = i;
    end
end
missedframes

%% Output creation
% Create output only if user asks
if output == 1 && trackcheck == 1
    % Save tr as textfile
    textfile = tr;
    textfile(:, 5) = radii_stack(1:length(textfile), 1); % can go wrong when
                                                    % multiple centers
                                                    % are involved

    fileID = fopen('save', 'w');
    fprintf(fileID, '%6.4f %6.4f %6.4f %6.4f %6.4f', textfile');
    fclose(fileID);
end
end

```

```
% If particle was tracked
if size(tr) > 0
    % Make new figure
    figure
    hold on
    box on
    % For number of particles in matrix tr
    for j = 1:max(tr(:, 4))
        % Define trj as the trajectory of a single particle
        trj = tr(find(tr(:, 4) == j), 1:3);
        % Plot trajectory
        plot(trj(:, 1), trj(:, 2), 'r-');
        % Label x-axis
        xlabel('X', 'FontSize', 20)
        % Label y-axis
        ylabel('Y', 'FontSize', 20)
        axis equal
    end
    hold off
end
% Save trajectory in corresponding folder
saveas(gcf, [directory name '_path.fig'])

%% Create contour for PIVlab
if PIVcheck == 1 && num_images ~= 1
    % This part of the code only works for a single particle
    % Create empty matrix PIV output
    PIV_output = [];
    % First two columns contain x and y position of particle (from pos)
    PIV_output(:, 1:2) = pos(:, 1:2);
    % Third column contains radius (from radiistack)
    PIV_output(:, 3) = radiistack(:, 1);
    l = length(PIV_output);
    ymask = NaN(1, l);
    xmask = NaN(1, l);
    for i = 1:l
        x = PIV_output(i, 1);
        y = PIV_output(i, 2);
        r = PIV_output(i, 3);
        % Create two new matrices with l points for the x- and y-
        % positions for a circular profile around the droplet center
        x1 = NaN(1, l);
        y1 = NaN(1, l);
        % Walk a circular path around the droplet center
        for j = 1:l
            x1(j) = x + cos(2*pi*j/l)*r;
            y1(j) = y + sin(2*pi*j/l)*r;
        end
        ymask(:, i) = y1;
        xmask(:, i) = x1;
    end
    % Save PIVlab mask in corresponding folder
    save([directory name '_contour.mat'], 'xmask', 'ymask');
end
```

Appendix C

Fabrication of the sedimentation sample well

Accessories

1. Four glass slides (Thermo Scientific Menzel-Gläser, 76 x 26 mm cut edges)
2. Glue (Griffon Combi Snel, 2-component epoxy glue)

A single glass slide is placed on a flat surface, and glue is carefully spread on both sides of about 1/4th of the glass width. Now two new glass slides are glued on top of the bottom slide, where about 3/4th of the two upper glass slides stick out on either sides. Additional glass slides can be put under the out sticking parts to stabilise the top slides until the glue has dried. When the glue has dried, the 4th glass slide is glued on top of the glass construction, placing it exactly above the bottom slide. When the glue has dried one of the sides of the slit is filled with glue closing the bottom to avoid any liquid be able to leak out. Remove the excess glue at the edges with ethanol and leave the sample well to dry.



Figure C.1: The sample well used for the sedimentation experiments in Chapter 2

Appendix D

The relation between Navier-Stokes and Reynolds

We start off writing down the Navier-Stokes equation D.1 (from which its solutions describe fluid flow fields) for an incompressible Newtonian fluid, that is a fluid which has a constant density. These types of fluid flows gives rise to viscous stresses proportional to the rate of shear strain. Those two main prerequisites are important as the validity of the formula below is merely applicable to this type of fluid, an example of a Newtonian fluid is a (diluted) aqueous surfactant solution.

To obtain a more general description it is often useful to nondimensionalise an equation. This allows for adjustment according to the parameters involved in ones system. An explicit way of nondimensionalising of the Navier-Stokes equation involves the vector notation of the equation written in Cartesian coordinates, as this form collapsed to a single equation and allows for fewer derivation steps.

$$\rho \frac{D\vec{u}}{Dt} = \rho \left(\frac{\partial \vec{u}}{\partial t} + \vec{u} \vec{\nabla} \vec{u} \right) = \rho \left(\frac{\partial \vec{u}}{\partial t} + u \frac{\partial \vec{u}}{\partial x} + v \frac{\partial \vec{u}}{\partial y} + w \frac{\partial \vec{u}}{\partial z} \right) = -\vec{\nabla} p + \rho \vec{g} + \eta \nabla^2 \vec{u} \quad (\text{D.1})$$

To be able to cancel out specific dimensions in our equation we need to provide a set of characteristic parameters of the same units as the scales in the equation, leading to a new set of parameters that are inherently unitless and therefore independent of the unit system. For clarity the dimensionless parameters are denoted in grey with an asterisk.

For the directions we define a characteristic length L and each of those directions is non-dimensionalised by dividing through that length, $x^* = \frac{x}{L}$, $y^* = \frac{y}{L}$, $z^* = \frac{z}{L}$. Since the nabla and the Laplace operators have dimensions of per unit length, multiplication needs to be done for the operators to become unitless; $\vec{\nabla}^* = L \vec{\nabla}$ and $\nabla^{*2} = L^2 \nabla^2$ respectively.

Furthermore we have to deal with time, velocity and pressure, which become dimensionless by defining some new quantities: U and t_{ref} , a characteristic velocity and a reference time respectively. This reference time needs to be the fastest time scale in the "problem" but can for steady boundary conditions be expressed as $t_{ref} = \frac{L}{U}$. The unitless counterparts associated with the remaining variables can then be expressed as: $\vec{u}^* = \frac{\vec{u}}{U}$, $t^* = \frac{t}{t_{ref}} = \frac{Ut}{L}$, $p^* = \frac{pL}{\eta U}$ and $\vec{g}^* = \frac{\vec{g}L}{U^2}$, and can be found in this form of the equation.

$$\frac{U^2 \rho}{L} \left(\frac{\partial \vec{u}^*}{\partial t^*} + \vec{u}^* \vec{\nabla}^* \vec{u}^* - \vec{g}^* \right) = \frac{U \eta}{L^2} \left(-\vec{\nabla}^* p^* + \nabla^{*2} \vec{u}^* \right)$$

We substituted the introduced parameters (for example $\vec{u} = \vec{u}^* U$) into the vector form of the Navier-Stokes equation and for simplicity rearranged the variables in such manner than we can clearly see the resemblance to the original equation. Multiplying both sides of the newly obtained equation with $\frac{L^2}{U \eta}$ and dropping the asterisks in the final form we arrived at the nondimensionalised version of the Navier-Stokes equation D.2 where the factor $\frac{UL}{\eta}$ happens to be the Reynolds number.

$$\frac{\rho UL}{\eta} \left(\frac{\partial \vec{u}}{\partial t} + \vec{u} \vec{\nabla} \vec{u} - \vec{g} \right) = \text{Re} \left(\frac{\partial \vec{u}}{\partial t} + \vec{u} \vec{\nabla} \vec{u} - \vec{g} \right) = -\vec{\nabla} p + \nabla^2 \vec{u} \quad (\text{D.2})$$

The dimensionless Reynolds number (Re) appears when we nondimensionalise the Navier-Stokes equations and this is a ratio between the inertial forces (ρUL) and the viscous forces (η). The Reynolds number is in the equation multiplied by the inertial term whereas the viscous term is present on the right. Effectively this means that when the Reynolds number is very small, inertial forces can be neglected meaning that viscous forces dominate the movement of our active particles.

In most derivations the gravitational acceleration term is left out as it can be assumed that the convective forces are much larger than the gravitational ones, but in terms of the derivation it can be considered and for completeness we take it into account here. Also note that in the final form of equation D.2 the viscosity term in front of the Laplace operator is missing, which is a consequence of our choice for the dimensionless pressure term, $p^* = \frac{pL}{\eta U}$ instead of $p^* = \frac{p}{\rho U^2}$ as would be the choice for larger values of the Reynolds number.

For large Reynolds numbers inertial forces dominate, which give rise to behavior that goes beyond the scope of this thesis, since the active particles studied here are in the low Reynolds regime. In the low Reynolds limit ($\text{Re} \ll 1$) equation D.2 collapses into the much easier Stokes equation, where the inertial forces are negligible. Commonly, the form including the viscosity term is displayed, but to keep in line with our derivation it is left out here.

$$\vec{\nabla} p = \nabla^2 \vec{u} \quad (\text{D.3})$$

Appendix E

Flow velocities in microfluidic devices

Solving the dimensional form of the Stokes equation (so including the viscosity term) for laminar creeping flow through a tube leaves us with an expression for the average flow velocity;

$$\langle \vec{u} \rangle = \frac{R^2}{8\eta} \frac{\Delta p}{L} \quad (\text{E.1})$$

where Δp is the pressure drop over the length L of the capillary and R the radius of the tube [29]. The volumetric flow rate Q is given by the average flow velocity times a cross-sectional area A_c of the tube. Since our devices consist of different shaped capillaries (square and round) two distinct expressions for the volumetric flow rate have to be given. The dispersed phase flows through the innermost capillary, that typically is a (tapered) round capillary through which the volumetric flow rate is given by Poiseuille's law.

$$Q = \langle \vec{u} \rangle \cdot \pi R^2 = \frac{\pi R^4}{8\eta} \frac{\Delta p}{L} \quad (\text{E.2})$$

In the main text in figure 2.5 an illustrative drawing of the type of microfluidic device used in this research is shown. Poiseuille accounts for the dispersed oil flow, whereas the continuous surfactant solution flow will be dealt with shortly as the capillary shape is of importance. The principle of controlled production of monodisperse droplets lies in the two shearing fluids. The oil flow through the innermost capillary results in droplet growth at the tip of the tapered capillary. This droplet grows until it has reached a certain size where the shearing force of the continuously shearing water-surfactant flow exceeds the balance between cohesive and adhesive forces that lie on the basis of droplet formation.

The continuous flow rate through the outermost capillary (typically a square capillary) is slightly more complicated. For the description of flow through a square capillary we will introduce the hydraulic diameter $D_H = 4A_c/P$, that is defined as 4 times the cross-sectional area divided by its (wetted) perimeter P . This hydraulic diameter allows us to describe different shaped channels by using a single parameter, a useful feature for non-dimensionalisation, but more importantly a parameter present in the Darcy-Weisbach equation, that provides a relation between the square of the average velocity and the pressure drop in an arbitrary shaped channel.

The Darcy-Weisbach relation is equated as:

$$\langle \vec{u} \rangle^2 = \frac{2D_H}{f_D \rho} \frac{\Delta p}{L} = \frac{2D_H \text{Re}}{k \rho} \frac{\Delta p}{L} \quad (\text{E.3})$$

where f_D is the Darcy friction factor, a dimensionless factor that accounts for the friction losses in all types of channel flow. For laminar flow in a tube the friction factor is related to the Reynolds number by a geometrical factor k , a numerical value that accounts for the shape of the channel,

related to the friction factor as $f_D = k/\text{Re}$. In table E.1 some geometric factors for laminar flow are listed, and substitution of this relation into the Darcy-Weisbach equation can be found on the right-hand side of equation E.3.

Table E.1: Numerical values for the geometric factor k , taken from the Nuclear Power website [2].

Geometric factor k	
Square	56.91
2:1 Rectangle	62.19
Circular	64.00
5:1 Rectangle	76.28
Parallel plates	96.00

When the Reynolds number is written down in terms and we take the characteristic velocity to be the average flow velocity and the characteristic length to be the hydraulic diameter, we arrive at the following expression for the average flow velocity:

$$\langle \vec{u} \rangle = \frac{2D_H^2}{k\eta} \frac{\Delta p}{L} \quad (\text{E.4})$$

Note that this expression equals Poiseuille's law when a circular tube is considered, as then $D_H = 4\pi R^2/2\pi R = 2R$ is substituted times the cross-sectional area of the tube (πR^2). In the case of a square tube the volumetric flow rate is written as

$$Q = \frac{D_H^4}{28.455\eta} \frac{\Delta p}{L}. \quad (\text{E.5})$$

Since the surfactant solution flowing through our microfluidic devices go from a wider outermost capillary through a narrower middle capillary, the velocity through the thinner tube will increase as is equated by Bernoulli:

$$\frac{1}{2}\rho\vec{u}^2 + \rho\vec{g}h + p = \text{constant} \quad (\text{E.6})$$

The Bernoulli equation is valid for incompressible fluids where $\frac{1}{2}\rho\vec{u}^2$ is the kinetic energy density, $\rho\vec{g}h$ the hydrostatic pressure (or potential energy) at a certain difference in height h , and p the pressure at a chosen point along the streamline. Therefore what the Bernoulli equation described, is simply the conservation of energy of fluid flow through a pipe.

